Title

The Autism-Associated Gene Scn2a Contributes to Dendritic Excitability and Synaptic Function in the Prefrontal Cortex.

Journal

Neuron, 103(4)

ISSN

0896-6273

Authors

Spratt, Perry WE
Ben-Shalom, Roy
Keeshen, Caroline M
et al.

Publication Date

2019-08-01

DOI

10.1016/j.neuron.2019.05.037

Peer reviewed

HHS Public Access

Author manuscript

Neuron. Author manuscript; available in PMC 2021 March 05.

Published in final edited form as:

Neuron. 2019 August 21; 103(4): 673–685.e5. doi:10.1016/j.neuron.2019.05.037.

The autism-associated gene *Scn2a* contributes to dendritic excitability and synaptic function in prefrontal cortex

Perry WE Spratt[*,1,2], **Roy Ben-Shalom**[*,1,2], **Caroline M Keeshen**[1,2], **Kenneth J Burke Jr.**[1,2], **Rebecca L Clarkson**[1,2], **Stephan J Sanders**[1,3], **Kevin J Bender**[1,2]

[1]Weill Institute for Neurosciences, University of California, San Francisco

[2]Department of Neurology, University of California, San Francisco

[3]Department of Psychiatry, University of California, San Francisco

Abstract

Summary: Autism spectrum disorder (ASD) is strongly associated with *de novo* gene mutations. One of the most commonly affected genes is *SCN2A*. ASD-associated *SCN2A* mutations impair the encoded protein $Na_V1.2$, a sodium channel important for action potential initiation and propagation in developing excitatory cortical neurons. The link between an axonal sodium channel and ASD, a disorder typically attributed to synaptic or transcriptional dysfunction, is unclear. Here, we show $Na_V1.2$ is unexpectedly critical for dendritic excitability and synaptic function in mature pyramidal neurons, in addition to regulating early developmental axonal excitability. $Na_V1.2$ loss reduced action potential backpropagation into dendrites, impairing synaptic plasticity and synaptic strength, even when $Na_V1.2$ expression was disrupted in a cell-autonomous fashion late in development. These results reveal a novel dendritic function for $Na_V1.2$, providing insight into cellular mechanisms likely underlying circuit and behavioral dysfunction in ASD.

eTOC Paragraph: Haploinsufficiency in the gene *SCN2A*, which encodes the sodium channel $Na_V1.2$, has strong autism association. Spratt et al. show that *Scn2a* contributes to dendritic excitability in mature neocortical pyramidal cells, where its loss impairs excitatory synaptic function and plasticity.

Graphical abstract

Corresponding author and lead contact: Kevin J. Bender, kevin.bender@ucsf.edu.

*equal contribution

Author contributions: Conceptualization: PWES, RBS, SMS, KJB; Methodology: PWES, RBS, KJB; Software: PWES, RBS, KJB Jr, RLC; Formal Analysis: PWES, RBS, CMK, KJB; Investigation: PWES, RBS, CMK, KJB Jr, KJB; Resources: SMS, KJB; Writing—original draft: PWES, KJB; Writing—review & editing: all authors; Visualization: PWES, RBS, KJB; Supervision: KJB; Project Administration: SMS, KJB; Funding Acquisition: PWES, RBS, SMS, KJB.

Declaration of interests: none declared.

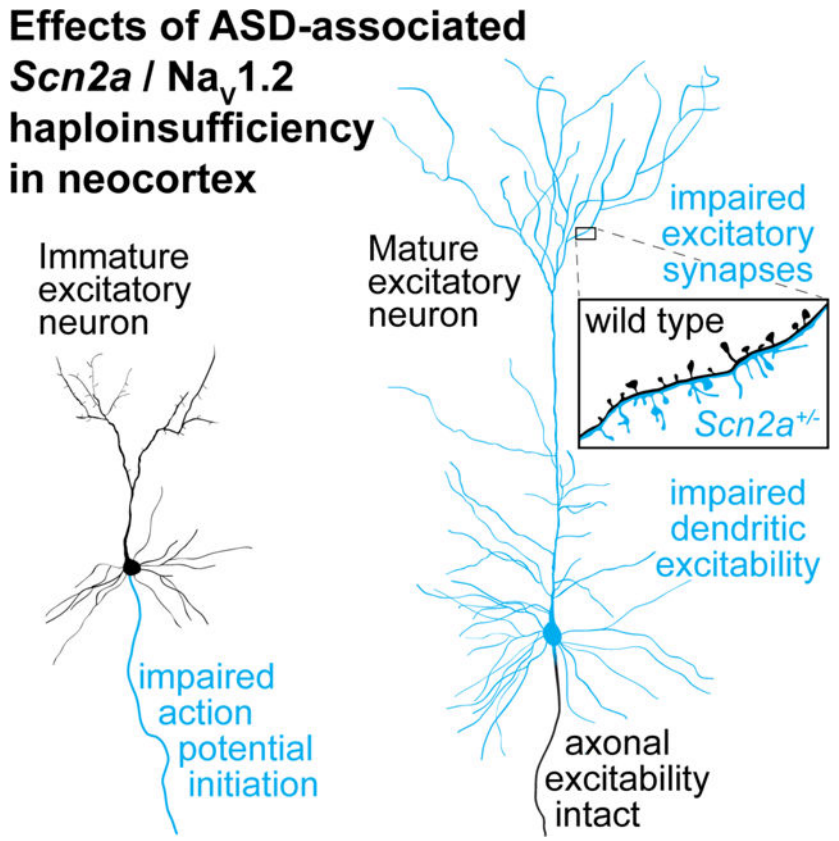

Introduction:

High-throughput sequencing has implicated numerous genes in autism spectrum disorder (ASD) (Sanders et al., 2015). These genes cluster into two groups: chromatin modifiers and genes that support synaptic function (De Rubeis et al., 2014; Sanders et al., 2015). Surprisingly, *SCN2A*, the gene with the most robust ASD association (Ben-Shalom et al., 2017; Sanders et al., 2012; Satterstrom et al., 2018), does not readily fit within either group. *SCN2A* encodes the protein $Na_V1.2$, a voltage-gated sodium channel known to be expressed in the axon initial segment (AIS), an axonal subcompartment adjacent to the soma that is the site of action potential (AP) initiation (Bender and Trussell, 2012; Kole and Stuart, 2012). Interestingly, *SCN2A* variants with different effects on channel function are associated with distinct neurodevelopmental disorders. Heterozygous loss of function variants (haploinsufficiency) in *SCN2A* that diminish or eliminate channel function are strongly associated with ASD as well as intellectual disability (ID), whereas gain of function missense variants are strongly associated with infantile epilepsy of varying severity (Begemann et al., 2019; Ben-Shalom et al., 2017; Sanders et al., 2018; Wolff et al., 2017). While neuronal hyperexcitability due to gain-of-function *SCN2A* variants likely contributes to infantile epilepsy, the neuropathological mechanisms underlying the strong association between *SCN2A* loss of function and ASD/ID remains largely unknown.

In neocortex, $Na_V1.2$ is primarily expressed in glutamatergic pyramidal cells (Hu et al., 2009; Li et al., 2014; Yamagata et al., 2017), where its distribution within different axonal compartments changes over development. In the first postnatal week in mice, corresponding to late gestation through the first year of life in humans (Workman et al., 2013), $Na_V1.2$ is the only sodium channel isoform expressed in the axon and AIS, and is thus solely responsible for the initiation and propagation of action potentials (Gazina et al., 2015). Later in development, $Na_V1.2$ in the axon and distal AIS is replaced by $Na_V1.6$ (*SCN8A*), which has a lower voltage threshold for activation (Bender and Trussell, 2012; Kole and Stuart, 2012). Consequently, the distal AIS becomes the site of AP initiation and $Na_V1.2$, now restricted to the proximal AIS, is thought to promote effective backpropagation of APs from the AIS into the soma (Hu et al., 2009). Given these potentially distinct developmental roles, it is critical to understand how *SCN2A* haploinsufficiency affects neuronal excitability and network function across development, as this may shed light on ASD and ID etiology.

Here, we examined cellular, synaptic, and behavioral consequences of heterozygous loss of *Scn2a* in mice ($Scn2a^{+/-}$). AP initiation was impaired in early development, consistent with a major role for *Scn2a* in axonal excitability. Unexpectedly, we identified deficits in somatodendritic excitability, consistent with the expression of $Na_V1.2$ channels throughout these compartments, that arose after early development and persisted throughout life. Furthermore, postsynaptic features of excitatory synapses on $Scn2a^{+/-}$ neurons were both functionally and structurally altered in adulthood, with morphological and electrophysiological features reminiscent of less mature synapses. Synaptic impairments were found even when *Scn2a* expression was disrupted late in development, selectively impairing dendritic excitability without a period of reduced axonal excitability. Reduced dendritic excitability impaired the backpropagation of action potentials into distal dendrites, with corresponding deficits in spike-timing dependent plasticity. Finally, we observed sex-specific trends toward deficits in learning and sociability in $Scn2a^{+/-}$ mice. Together, these results identify a novel role for $Na_V1.2$ in the dendrites of mature pyramidal neurons, demonstrating that $Na_V1.2$ contributions to dendritic, and not only axonal, excitability are important for proper synaptic development and function. This generates the hypothesis that *SCN2A* contributes to ASD and ID by disrupting synaptic function, like many other ASD genes, and that these effects persist in mature neurons.

Results:

Scn2a loss impairs axonal and dendritic excitability in distinct developmental periods.

To determine how *Scn2a* haploinsufficiency affects cortical neuron excitability, acute slices containing medial prefrontal cortex (mPFC) were prepared from $Scn2a^{+/-}$ and wild-type (WT) littermate control mice aged postnatal day (P)4 through P64. $Scn2a^{+/-}$ mice have a 50% reduction in $Na_V1.2$ mRNA, have reduced Na_V-mediated currents in dissociated cell culture at P5–9 (Planells-Cases et al., 2000), and are convulsive-seizure free (Mishra et al., 2017; Ogiwara et al., 2018), consistent with the majority of *Scn2a* loss-of-function cases reported in ASD (Sanders et al., 2018). We focused our studies primarily on subcortically projecting layer 5b thick-tufted neurons that were identified based on electrophysiological properties (Clarkson et al., 2017; Dembrow et al., 2010; Gee et al., 2012) (see Methods), as

dysfunction within this region and cell class has been implicated in ASD (Willsey et al., 2013). Neuronal excitability was assessed using a series of current steps to generate APs. AP threshold was depolarized and spike output was reduced relative to WT in the first postnatal week (Fig. 1A, C, F). Differences between *Scn2a*$^{+/-}$ and WT were not present thereafter (Fig. 1B, C, F), consistent with increased $Na_V1.6$ expression in the AIS. In agreement, persistent sodium currents, which reflect the recruitment of AIS sodium channels with the lowest threshold (Taddese and Bean, 2002), were suppressed in *Scn2a*$^{+/-}$ mice at P6, but not at P30 (Fig. S1A–G). Furthermore, axonal conduction, assayed by imaging AP-evoked calcium transients in boutons, was reliable in both immature and mature neurons (Fig. S2). Input resistance was comparable between *Scn2a*$^{+/-}$ and WT at all ages, and transient and sustained potassium currents were not different in both immature and mature neurons (Fig. S1H–K). Therefore, *Scn2a* haploinsufficiency impairs neuronal excitability early in development without functional compensation from the remaining *Scn2a* allele or other ion channels involved in AP initiation.

Although impairments in AP threshold recovered after P7, a closer examination of the AP waveform revealed a striking reduction in the velocity of the AP (dV/dt) that became more pronounced as neurons matured (Fig. 1E–F) (>P22, WT: 578.2 ± 9.2 V/s, n = 44 cells; *Scn2a*$^{+/-}$: 417 ± 9.5, n = 33 cells; $p < 0.001$, Mann-Whitney). Similar relative deficits were identified in putative thin-tufted neurons, which have different AP waveform characteristics compared to thick-tufted neurons (Dembrow et al., 2010) (>P18: WT: 426.9 ± 24.7 V/s, n = 8 cells; *Scn2a*$^{+/-}$: 358 ± 21.1, n = 9 cells; $p = 0.007$, Mann-Whitney). Plotting AP velocity as a function of voltage (phase-plane) highlights two components of the rising phase of the AP (Fig. 1D), as measured with somatic current-clamp. The first relates to the initiation of the AP in the AIS and the second to the recruitment of somatic sodium channels (Bean, 2007). In *Scn2a*$^{+/-}$ cells, both AIS and somatodendritic components of the AP were slower, suggesting that $Na_V1.2$ channels are distributed in both the AIS and somatodendritic compartment, and that their density is lower in both compartments. Similar AP speed deficits were observed in pyramidal cells located in other neocortical regions, including medial orbitofrontal cortex and primary visual cortex (Fig. S3A–D). In contrast to neocortical neurons, no alterations in AP threshold and peak speed were apparent in hippocampal CA1 pyramidal neurons (Fig. S3E–F). This is consistent with immunostaining indicating that hippocampal pyramidal cell dendrites predominantly express $Na_V1.6$ (Lorincz and Nusser, 2010).

Immunostaining for $Na_V1.2$ in neocortex suggests that $Na_V1.2$ channels are predominantly localized to excitatory neurons, with little to no membrane localization observed in parvalbumin or somatostatin positive interneurons (Li et al., 2014; Yamagata et al., 2017). These cell classes instead express $Na_V1.1$ channels, and exhibit hypoexcitability in *Scn1a* haploinsufficient mice aged P14–21 (Favero et al., 2018; Tai et al., 2014). To further test whether $Na_V1.2$ contributes to AP excitability in these interneuron classes, we crossed *Scn2a*$^{+/+}$ and *Scn2a*$^{+/-}$ mice to mice engineered to express tdTomato in either parvalbumin or somatostatin positive cells (see Methods). Fluorescently guided whole-cell current-clamp recordings were then made from these populations in slices prepared from P34–40 animals (Fig. 2). Though AP waveforms differed across cell class, neither peak dV/dt (Fig. 2; PV peak dV/dt: WT: 336 ± 19 V/s, n = 9 cells, *Scn2a*$^{+/-}$: 326 ± 21 V/s, n = 9 cells; SOM peak

dV/dt: WT: 362 ± 27 V/s, n = 12 cells, *Scn2a*$^{+/-}$: 313 ± 23 V/s, n = 11 cells; p = 0.43, $F_{genotype}(1,37) = 0.65$, 2-way ANOVA) or threshold (PV threshold: WT: −51.7 ± 1.6 mV, n = 9 cells, *Scn2a*$^{+/-}$: −51.9 ± 0.7 mV, n = 9 cells; SOM threshold: WT: −39.7 ± 0.7 mV, n = 12 cells, *Scn2a*$^{+/-}$: −41.6 ± 1.0 mV, n = 11 cells; p = 0.41, $F_{genotype}(1,37) = 0.68$, 2-way ANOVA) were affected by loss of $Na_V1.2$.

Overall, these data indicate that *Scn2a* haploinsufficiency alters the excitability of neocortical pyramidal cells, but not parvalbumin or somatostatin positive interneurons. Furthermore, within pyramidal cells, $Na_V1.2$ channels may be more consequential for somatodendritic excitability than axonal excitability. To explore the cellular consequences of reduced somatodendritic excitability, we modified an established computational model of cortical pyramidal cells (Hallermann et al., 2012) by varying the localization and relative density of $Na_V1.2$ and $Na_V1.6$ (Ben-Shalom et al., 2017). First, $Na_V1.2$ channels were localized only to the AIS, and AP waveform was compared between models with 100% and 50% $Na_V1.2$ expression (Fig. 3A). AP waveform was only modestly altered by such manipulations. To best account for empirical observations, we found that $Na_V1.2$ expression was required throughout the somatodendritic compartment, in equal levels with $Na_V1.6$ (Fig. 3A, Fig. S4A–B, D–E). In this configuration, we modeled AP waveform throughout the dendritic arbor and found that backpropagating APs (bAPs) from the AIS to the dendritic arbor were attenuated in a distance dependent fashion. Though AP amplitudes were reduced only 10% in the soma, they were attenuated to far greater extents in distal dendrites (41% of WT amplitude in distal tuft) (Fig. 3B, Fig. S5D), suggesting that cellular processes that depend on bAPs may be altered in *Scn2a*$^{+/-}$ cells.

Backpropagating APs can provide instructive signals for dendritic integration and synaptic plasticity, largely through their ability to elicit calcium influx through dendritic voltage-dependent calcium channels and NMDA receptors (Feldman, 2012; Larkum et al., 1999a; Stuart and Häusser, 2001). To determine whether bAP-associated dendritic excitability was impaired in *Scn2a*$^{+/-}$ neurons, we imaged calcium transients evoked by trains of high-frequency bursts (2APs at >100Hz) at various locations throughout the apical dendrite of layer 5 pyramidal cells. Bursts of APs, rather than single APs, were chosen because they have been shown to evoke dendritic calcium transients throughout apical dendrites, including distal tuft regions (Barth et al., 2008; Gulledge and Stuart, 2003; Larkum et al., 1999b; Short et al., 2017). In WT neurons, bursts reliably evoked calcium transients throughout the apical dendrite. By contrast, calcium transients in *Scn2a*$^{+/-}$ neurons rapidly diminished in amplitude with increasing distance from the soma, becoming virtually absent in the most distal dendritic branches (Fig. 3C–D). To determine whether these effects were due to acute loss of Na_V channels, rather than a consequence of altered excitability during development, we partially blocked sodium channels in mature WT neurons with tetrodotoxin (TTX), using a concentration that mimicked the reduced AP speed observed in *Scn2a*$^{+/-}$ neurons (5 nM, Fig. S4G–H). Consistent with acute effects of *Scn2a* haploinsufficiency, bAP-evoked calcium transients were reduced to a comparable extent in TTX-exposed WT neurons (Fig. 3C–D). Thus, *Scn2a*$^{+/-}$ haploinsufficiency leads to a major, persistent deficit in dendritic excitability in adult L5 neurons that is likely due to loss of $Na_V1.2$ channels localized to the dendrite.

Excitatory synapses are impaired in mature *Scn2a*$^{+/-}$ neurons.

Impairments of both axonal and dendritic excitability could affect synapses, which are a common locus of dysfunction in mouse models of ASD (Bourgeron, 2015; Monteiro and Feng, 2017; Tsai et al., 2012). We tested this by first measuring miniature excitatory and inhibitory postsynaptic currents (mEPSC, mIPSC) at P6 and P27, capturing developmental periods of axonal and dendritic excitability deficits, respectively. Neither mEPSCs nor mIPSCs were affected at P6. At P27, mEPSC frequency was reduced by 48% (WT: 9.3 ± 1.1 Hz, n = 23 cells; Scn2a$^{+/-}$: 4.9 ± 0.8, n = 19 cells; $p < 0.001$ Mann-Whitney), with no change in mEPSC amplitude (Fig. 4A–B) or mIPSC amplitude or frequency (S6A–B).

Lower mEPSC frequencies could reflect reductions in release probability or the number of functional synapses contributing to AMPA-mediated mEPSCs. The paired pulse ratio, which is sensitive to differences in release probability, was not different between *Scn2a*$^{+/-}$ and WT cells (Fig. 4C, S5C–D). By contrast, the ratio of AMPA- to NMDA-mediated current in evoked EPSCs was reduced in *Scn2a*$^{+/-}$ cells (Fig. 4D; WT: 5.5 ± 0.7, n = 8 cells: *Scn2a*$^{+/-}$: 3.2 ± 0.2, n = 12 cells; $p < 0.01$, Mann-Whitney). Taken together, the reduction in both mEPSC frequency and AMPA:NMDA ratio suggest that mature *Scn2a*$^{+/-}$ neurons have an excess of AMPA-lacking spines that are more commonly observed at earlier developmental time points (Hanse et al., 2013; Kerchner and Nicoll, 2008).

Consistent with these functional observations, dendritic spine morphology was also altered in mature, but not immature, *Scn2a*$^{+/-}$ cells, though overall dendritic arbor structure was unaltered (Fig. 5A–B). At P5–6, filipodial spines identified on developing apical dendrites were similar in morphology and density in wildtype and *Scn2a*$^{+/-}$ neurons (Fig. 5C–D). In more mature neurons (>P23), spine density was comparable between WT and *Scn2a*$^{+/-}$ on both apical and basal dendrites; however, *Scn2a*$^{+/-}$ spines were longer and had smaller heads relative to their total head and neck volume (Fig. 5C–D), thus sharing features with spines more commonly found in less mature cells.

To determine whether impaired synaptic function was due to early developmental deficits in axonal excitability or persistent deficits in dendritic excitability, we engineered a mouse with one *Scn2a* allele under Cre-loxP control (*Scn2a*$^{+/fl}$) (Fig. S6A). Mice were first crossed to the CaMKIIα-Cre driver line, which expresses Cre in neocortical pyramidal cells only after P10 (Fig. S6B, Xu et al., 2000). As such, *Scn2a*$^{+/fl}$::CaMKIIα-Cre mice develop with normal AP threshold and spike output. In *Scn2a*$^{+/fl}$::CaMKIIα-Cre mice, peak dV/dt was not different at P18, likely due to a combination of low Cre expression and slow $Na_V1.2$ turnover. By P50, peak dV/dt matched constitutive *Scn2a*$^{+/-}$ neurons (Fig. 6B). Furthermore, bAP-evoked dendritic Ca transients were suppressed to comparable extents as observed in constitutive *Scn2a*$^{+/-}$ mice (Fig. 6C–D). Thus, these mice developed without early deficits in axonal excitability and exhibited impaired dendritic excitability only later in development.

Strikingly, AMPA:NMDA ratio was reduced in *Scn2a*$^{+/fl}$::CaMKIIα-Cre neurons when measured after P50, revealing that impaired dendritic excitability alone is sufficient to alter synapse strength (Fig. 6E; WT: 4.2 ± 0.3, n = 12 cells; floxed: 2.5 ± 0.4, n = 11 cells; $p < 0.01$, Mann-Whitney). To test whether these synaptic deficits result from a cell-autonomous loss of *Scn2a*, we injected a dilute Cre-expressing adeno-associated virus (AAV-EF1α-Cre-

mCherry) into mPFC of P28 *Scn2a*$^{+/fl}$ mice (Fig. 6A). Four weeks later, we found that both peak dV/dt and AMPA:NMDA ratio were reduced in Crepositive, but not Cre-negative neurons (Fig. 6B, E; WT: 5.0 ± 0.4, n = 10 cells; floxed: 2.4 ± 0.4 n = 9 cells; $p < 0.01$, Mann-Whitney). Modest increases in spine length were also noted in spines along the apical dendrites of *Scn2a*$^{+/fl}$::CaMKIIα-Cre cells (Fig. S7). These results indicate that the persistent, cell-autonomous, dendritic function of $Na_V1.2$ is required to maintain aspects of normal synaptic function in mature pyramidal cells.

These changes in synapse structure and function could arise if synapses lack instructive signals for maintaining synaptic strength. Indeed, physiologically relevant forms of synaptic plasticity depend on the coincident detection of bAPs and glutamate at the synapse, a process that may be affected in *Scn2a*$^{+/-}$ cells (Feldman, 2012; Magee and Johnston, 1997; Markram et al., 1997, 2012). To test whether plasticity is impaired in these cells, we induced long-term potentiation (LTP) of putative apical dendrite synapses by pairing layer 1 fiber stimulation with bursts of APs (Fig. 7A, Kampa et al., 2006; pairing protocol: Tzounopoulos et al., 2004). In WT neurons, paired stimulation resulted in long-lasting synaptic potentiation. In contrast, LTP was not observed in either *Scn2a*$^{+/-}$ neurons or in WT neurons in 5 nM TTX (Fig. 7B–D, EPSP slope, normalized to baseline: WT: 1.52 ± 0.10, n = 11 cells; *Scn2a*$^{+/-}$: 0.98 ± 0.11, n = 11 cells; TTX: 0.97 ± 0.06, n = 9 cells; $p = 0.0002$, Kruskal-Wallis test; WT vs *Scn2a*$^{+/-}$: $p = 0.0007$, WT vs TTX: $p = 0.002$, Dunn's multiple comparisons test). Thus, *Scn2a* haploinsufficiency impairs synaptic plasticity, consistent with impairments in bAP-evoked calcium transients in the dendrites.

Scn2a$^{+/-}$ mice have trends towards deficits in learning and social behavior

Given these physiological deficits and the association of loss-of-function *SCN2A* mutations with ASD and ID in humans, we next asked if *Scn2a* haploinsufficiency results in corresponding behavioral impairments in mice. As mouse models harboring other ASD-associated genetic variants exhibit a range of behavioral differences (Pasciuto et al., 2015; Silverman et al., 2010), we screened *Scn2a*$^{+/-}$ mice and WT littermates of both sexes (5–13 mice per sex and genotype combination) through a behavioral panel designed to assess locomotion, anxiety, repetitive behavior, sociability, and learning (Fig. S8). In total, 10 assays were performed yielding 30 metrics that we assessed for genotypic differences. While no individual metric differed significantly between the wildtype and heterozygote mouse after correcting for multiple comparisons, we observed a trend towards impaired reversal learning in a water T-maze task in males (Fig. S8A). In this task, mice must first learn which arm of a maze contains a submerged platform (day 1–4, 4 trials/day), then reverse their association when the platform location is switched (day 5–8, 6 trials/day). A replication experiment of two further batches of male (23 vs. 24 mice total) and female (20 vs. 24 mice total) *Scn2a*$^{+/-}$ and WT littermates showed a similar trend toward reversal learning impairments (Fig. S9A, $p = 0.026$, $F_{Genotype}$ (1, 45) = 5.2, 2-way repeated measures ANOVA; alpha required for multiple comparisons in replication cohort: 0.003), while no trends were observed in females.

We also observed trends suggestive of social impairments in female mice (Fig. S9B–D). Specifically, in our initial screen we observed no difference in social approach behavior in a

two-chamber social task, where mice had the option of interacting with a caged, sex-matched stimulus mouse in one chamber or an inanimate toy mouse in the other (Fig. S8B). In a second cohort, mice were paired with the same stimulus mouse for three trials to assess social approach and habituation. Both sexes and genotypes showed a comparable preference to the stimulus mouse vs the toy mouse across the three trials (Fig. S8B). Given the importance of social interaction in ASD, we also tested interactions when the toy mouse was replaced with a novel stimulus mouse on the fourth trial. Both male and female WT mice switched preference to the new stimulus mouse whereas female *Scn2a*$^{+/-}$ mice showed no preference for the novel mouse (Δinteraction time*:*, *Scn2a*$^{+/+}$: −17.1 ± 4.1 sec, n = 13 mice; *Scn2a*$^{+/+}$: 9.3 ± 10.3 sec, n = 8 mice, p = 0.017; Mann-Whitney) (Fig. S9D). Female *Scn2a*$^{+/-}$ mice were also found to enter the open arms of the elevated plus maze more often (percent time in open arms: *Scn2a*$^{+/+}$: 22.9 ± 2.1%, n = 24 mice; *Scn2a*$^{+/+}$: 34.3 ± 2.7% sec, n = 20 mice, p = 0.002; Mann-Whitney), with a trend towards spending more time in these open arms (number of open arm entries: *Scn2a*$^{+/+}$: 56.6 ± 3.3, n = 24 mice; *Scn2a*$^{+/-}$: 73.6 ± 5.5 n = 20, p = 0.012; Mann-Whitney) (Fig. S9F). Overall, these data suggest that *Scn2a*$^{+/-}$ mice may display sex-specific impairments in behavioral flexibility and social discrimination.

Discussion:

Here, we report that $Na_V1.2$ channels contribute to excitatory synapse function through an unexpected role in dendritic excitability, and that cell-autonomous *Scn2a* haploinsufficiency late in development is sufficient to impair excitatory synaptic connectivity. This reframes *SCN2A* as a gene not only important for axonal excitability, but also for dendritic excitability in neocortical pyramidal neurons. *Scn2a* haploinsufficiency affects dendritic excitability throughout life, with corresponding deficits in synaptic function and plasticity that may be consequential for ASD/ID etiology.

$Na_V1.2$ channel expression in neocortical pyramidal cell dendrites

While the expression of $Na_V1.2$ in the AIS is well established (Gazina et al., 2015; Hu et al., 2009; Liao et al., 2010), there is less consensus on its distribution in pyramidal cell dendrites. The first immunostaining of $Na_V1.2$ in neocortex revealed somatic and apical dendritic localization in pyramidal cells, though this may represent a pool of newly synthesized channels within vesicles (Gong et al., 1999). Functionally, somatodendritic Na_V currents in neocortical pyramidal neurons are best described by $Na_V1.2$ channels (Hu and Bean, 2018; Hu et al., 2009). Here, we found that AP waveform was altered in constitutive and conditional *Scn2a*$^{+/-}$ prefrontal thick-tufted layer 5 pyramidal cells in a manner best explained by somatodendritic loss of $Na_V1.2$, with no functional compensation from the residual *Scn2a* allele or $Na_V1.6$ (Fig. 1–2, S1, S4). Similar observations were made in prefrontal thin-tufted layer 5 pyramidal cells, and in thick-tufted layer 5 pyramidal cells localized to orbitofrontal and primary visual cortex (Fig. S3). Moreover, AP-evoked calcium transients in PFC pyramidal neurons were suppressed throughout the dendritic arbor of *Scn2a*$^{+/-}$ cells (Fig. 3, 6), and this effect could be mimicked in wildtype neurons acutely by sub-saturating concentrations of TTX.

In mature hippocampal preparations, $Na_V1.2$ channels have been visualized in pyramidal cell initial segments, and also were co-localized with the presynaptic terminal marker VGlut1 in strata containing unmyelinated axons, but were not present in pyramidal cell dendrites (Lorincz and Nusser, 2010, but see Johnson et al., 2017). Consistent with this observation, AP waveform was not altered in recordings from CA1 hippocampal neurons (Fig. S3). This suggests that $Na_V1.2$ channels are selectively found in the dendrites of neocortical, but not archicortical, pyramidal cells. This hypothesis will require further work to measure dendritic excitability directly in hippocampal neurons, and to rule out compensation by other Na_V subtypes. Furthermore, there may be regional differences in expression in other neocortical regions between frontal and visual cortex, or in other laminae. Altogether, these data indicate that $Na_V1.2$ is functionally expressed in the soma and dendrites of neocortical pyramidal neurons, where they play an important role in excitability and synapse function.

Role of $Na_V1.2$ in dendritic and synaptic function

Scn2a haploinsufficiency selectively impairs dendritic excitability and synaptic function in mature PFC pyramidal cells, with no effects on AP initiation or propagation (Fig. 1, S2). This distinguishes $Na_V1.2$ from other Na_V isoforms expressed in the mature cortex that either support overall excitability in inhibitory neurons ($Na_V1.1$) or contribute to both action potential generation and dendritic excitability in pyramidal neurons ($Na_V1.6$) (Hu et al., 2009; Lorincz and Nusser, 2008; Ogiwara et al., 2007). In the mature brain, $Na_V1.2$ may instead play a major role in supporting the backpropagation of action potentials within neocortical pyramidal cell dendrites. These bAPs depolarize dendrites and can contribute to the generation of dendritic spikes, especially when paired with local synaptic stimulation (Larkum et al., 1999a), or when packaged in high-frequency bursts (Barth et al., 2008; Gulledge and Stuart, 2003; Larkum et al., 1999b). Here, we found that somatodendritic $Na_V1.2$ channels are critical for supporting bAPs from the AIS to the distal dendrites, and that *Scn2a* haploinsufficiency impairs the ability to induce a burst-based form of associative spike-timing dependent plasticity at apical tuft synapses (Figs. 3C–D, 5C, 7). Furthermore, excitatory synapse function was altered in ways most consistent with a postsynaptic, dendritic role for $Na_V1.2$ channels in mature neurons. Presynaptic metrics, including the likelihood of evoking calcium transients in axonal boutons and paired-pulse ratio, were unaffected by *Scn2a* loss (Fig. S2, S5). By contrast, miniature EPSC frequency and AMPA:NMDA ratio were reduced, consistent with the hypothesis that a higher proportion of silent synapses are present in $Scn2a^{+/-}$ cells (Fig. 4). These effects were mirrored by structural differences in spines imaged on basal and apical dendrites of more mature neurons (Fig. 5C–D). Interestingly, these functional and structural aspects were dissociable, as induction of *Scn2a* haploinsufficiency late in life reduced AMPA:NMDA ratio with little change in spine shape (Figs. 6E, S7). This is consistent with other cell- and circuit-based perturbations in more mature neurons, where synapse strength can be altered markedly with relatively small changes in spine morphology (Dobi et al., 2011; Sala et al., 2003; Shen et al., 2014), and suggests that certain aspects of spine morphology are developmentally regulated before the ages at which *Scn2a* loss was induced in $Scn2a^{+/fl}$ mice studied here.

While we focused on backpropagation of bursts and related plasticity in the tuft of *Scn2a*$^{+/-}$ cells, reductions in $Na_V1.2$ density likely affect many other dendritic processes. For example, dendrites are capable of generating spikes independent of APs at the AIS through multiple mechanisms, including Na_Vs (Kim et al., 2015; Stuart et al., 1997). These dendritic spikes alone can be instructive for synaptic plasticity (Golding et al., 2002; Kampa et al., 2007). Furthermore, plasticity mechanisms that influence synaptic strength in dendrites more proximal to the soma are also likely affected, given the structural changes observed in basal dendrites and in EPSCs evoked with electrical stimulation in layer 5. High-frequency burst-based stimuli used here readily produced calcium transients in proximal dendritic locations in *Scn2a*$^{+/-}$ cells. Other activity that drives dendritic calcium influx, including single APs or coordinated activation of excitatory inputs (Ariav et al., 2003), may instead be affected in these regions.

Measurements of persistent sodium current suggest that the loss of $Na_V1.2$ channels is not functionally compensated for by $Na_V1.6$. Consistent with this, mRNA for $Na_V1.6$, $Na_V1.1$, and Na_V beta subunits are unaltered in *Scn2a*$^{+/-}$ mice (Ogiwara et al., 2018). We also found no differences in transient or sustained potassium currents or input resistance, suggesting that other channel types are similarly unaltered by $Na_V1.2$ reductions. However, interpretation of this is hampered by the inability to adequately clamp these currents via somatic recording. While empirical measurements indicate that we have reasonable voltage control over persistent sodium currents in the AIS (Fig. S1E–G), other events, including synaptic activity and potassium currents, may suffer from incomplete voltage control in these large dendritic cells (Beaulieu-Laroche and Harnett, 2018; Williams and Mitchell, 2008). Importantly, voltage errors are likely comparable across genotype, since we do not observe differences in dendritic morphology, input resistance, and spine density (Figs. 5, S1). Furthermore, effects of $Na_V1.2$ loss on bAP-associated dendritic calcium transients were recapitulated by acutely blocking a small fraction of Na_Vs in WT cells. Thus, even though we have not assessed the function of ion channels in the apical tuft directly, our data are most easily explained by a reduction in $Na_V1.2$ alone, with no compensation from other Na_Vs or other ion channel classes.

Relationship with other ASD-associated genes

While *SCN2A*'s ASD association has been established for some time (Sanders et al., 2012), the mechanistic underpinnings of this strong association have been a mystery. Since $Na_V1.2$ channels were best understood for their role in AP initiation (Hu et al., 2009), it was difficult to find parallels with other ASD-associated genes that are associated with synaptic function and gene transcription (De Rubeis et al., 2014). Data shown here instead suggest that *SCN2A* function in ASD converges at the dendrite with the large group of ASD-associated genes involved in synaptic function. Indeed, disruptions in both excitatory synaptic function and neuronal excitability have been reported in other ASD-associated genes (Bateup et al., 2011; Bozdagi et al., 2010; Contractor et al., 2015; Greer et al., 2010; Meredith and Mansvelder, 2010; Nestor and Hoffman, 2012; Williams et al., 2015; Yashiro et al., 2009; Yi et al., 2016). How the other ASD-associated genes with roles in regulating gene expression mediate ASD risk remains unknown (Sanders, 2015), however we note that *SCN2A* has

been reported as a regulatory target of both FMRP and CHD8 (Darnell et al., 2011; Golden et al., 2019; Sugathan et al., 2014).

SCN2A was one of the first genes identified with a clear excess of missense mutations in addition to predicted protein truncating variants linked to ASD and ID (Ben-Shalom et al., 2017; Sanders et al., 2015). Recent efforts have identified other genes harboring ASD-associated missense variants, though the functional implications of such mutations are largely unclear (Geisheker et al., 2017). $Na_V1.2$ function, by contrast, can be well characterized, allowing for a better understanding of how missense mutations that alter channel activity affect neuronal function. Several recurring *SCN2A* missense variants block sodium flux (Begemann et al., 2019; Ben-Shalom et al., 2017). These may be functionally identical to protein truncating variants, since we and others find that $Na_V1.2$ function is reduced 50% in *Scn2a*$^{+/-}$ mice (Planells-Cases et al., 2000), with no evidence for functional compensation. Other *SCN2A* missense variants observed in ASD patients alter channel voltage dependence or kinetics, reducing neuronal excitability in models of developing cortical pyramidal cells (Ben-Shalom et al., 2017). Whether they result in similar dendritic deficits in mature neurons remains to be tested.

Role of *Scn2a* in learning and behavior

The behavioral differences observed thus far in heterozygous *Scn2a* mice parallel aspects of behavioral phenotypes reported in other mouse models of ASD-associated genes (Pasciuto et al., 2015; Silverman et al., 2010). Here, we observed trends toward impaired behavioral flexibility in males and impaired social recall and reduced anxiety in females. Reversal learning effects we observed in male mice parallel spatial learning impairments observed previously in male *Scn2a*$^{+/-}$ mice (Middleton et al., 2018). Whether female *Scn2a*$^{+/-}$ are similarly resistant to these specific spatial learning impairments has not been explored. Male *Scn2a*$^{+/-}$ mice were also recently found to display novelty-induced exploratory hyperactivity, social behavior impairment, enhanced fear conditioning, and deficient fear extinction (Tatsukawa et al., 2019). Of note, several phenotypic results, including open field, elevated plus maze, and social interaction, were not replicated here. This issue of reproducibility is unfortunately common in behavioral studies examining ASD-like phenotypes in mouse, and may relate to differences in genetic background, genetic drift over generations, or experimental conditions (Brunner et al., 2015; Chadman et al., 2008; Ey et al., 2012; Spencer et al., 2011).

Children with *SCN2A* loss-of-function variants display a range of phenotypes, including ASD, ID, and cortical visual impairments. Here, we found that neurons in visual cortex have similar deficits in AP waveform, possibly reflecting deficits in dendritic excitability that could impair visual processing (Xu et al., 2012). Furthermore, a fraction of these children also develop seizure phenotypes, typically after the first year of life (Sanders et al., 2018; Wolff et al., 2017). *Scn2a*$^{+/-}$ mice have been reported to be seizure free (Mishra et al., 2017; Planells-Cases et al., 2000), or to have low-frequency, short duration spike-wave discharges (Ogiwara et al., 2018). The variability of seizure occurrence in human and mouse suggests that factors other than *Scn2a* loss alone, including genetic background, may contribute to seizure susceptibility.

In conclusion, we found that haploinsufficiency induction at two different developmental timepoints, both well after $Na_V1.2$ channels cease to contribute to AP initiation, was sufficient to alter synaptic function (Fig. 3, 6). While this result does not exclude additional effects on network function due to reduced axonal excitability in early cortical development, it does indicate that proper $Na_V1.2$ function that supports dendritic excitability is required for maintaining synaptic strength. Thus, restoring proper $Na_V1.2$ function, even in the mature brain, may be an enticing avenue for therapeutic intervention in loss-of-function *SCN2A* cases.

STAR Methods:

CONTACT FOR REAGENT AND RESOURCE SHARING

Contact for Reagent and Resource Sharing—Requests for reagents and resources should be directed to Kevin Bender (kevin.bender@ucsf.edu)

EXPERIMENTAL MODEL AND SUBJECT DETAILS

All experimental procedures were performed in accordance with UCSF and Gladstone Institutes IACUC guidelines. All experiments were performed on mice housed under standard conditions with ad libitum access to food and water. C57B6J (JAX: 000664), B6.Cg-Tg(Camk2a-cre)T29–1Stl/J (Jax: 005359), Ai14: 6;129S6-Gt(ROSA)26Sortm14(CAG-tdTomato)Hze/J (JAX: 007908) were obtained from The Jackson Laboratory and bred in our onsite colony. *Scn2a*$^{+/-}$ mice were provided by Drs. E. Glasscock and M. Montal (Mishra et al., 2017; Planells-Cases et al., 2000). *Scn2a*$^{+/fl}$ mice were created by inserting LoxP sites around exon 2 of the *Scn2a* gene (Fig, S6A, Cyagen). A targeting vector was generated by PCR using BAC clone RP23–332C13 and RP24–42717 from the C57BL/6J library to create homology arms around a LoxP flanked cKO region that includes exon 2 of the *Scn2a* gene. The targeting vector included a Neo cassette flanked by Rox sites for positive selection, and DTA outside of the homology arms for negative selection. The linearized vector was subsequently delivered to ES cells (C57BL/6) via electroporation, followed by drug selection, PCR screening, and Southern Blot confirmation. Confirmed clones were then introduced into host embryos and transferred to surrogate mothers. Chimerism in the resulting pups was identified via coat color. F0 male chimeras were bred with C57BL/6 females to generate F1 heterozygous mutants that were identified by PCR.

Method Details

Ex Vivo Electrophysiology: Mice aged P4 through P62 were anesthetized, and 250 μm-thick coronal slices containing medial prefrontal cortex, medial orbitofrontal cortex, hippocampal CA1, or primary visual cortex (Fig. S3A) were prepared. Slices were prepared from *Scn2a*$^{+/-}$, CaMKII-Cre (MGI: 2446639)::*Scn2a*$^{+/fl}$, Parv-Cre (MGI: 3590684)::Ai14::*Scn2a*$^{+/-}$, SOM-Cre (MGI: 4838416)::Ai14::*Scn2a*$^{+/-}$, or *Scn2a* wild type littermates (genotyped by PCR). All data were acquired and analyzed blind to *Scn2a* genotype, except for experiments examining the effects of tetrodotoxin in a wild type background (AP waveform and synaptic plasticity), and the effects of sparse Cre transfection in *Scn2a*$^{+/fl}$ mice. Data were acquired from both sexes (blind to sex), with no sex-dependent

differences noted in measurements made in acute slice recordings [e.g., AMPA:NMDA ratio, combined data across constitutive and conditional heterozygote cases: Male +/+ 5.1 ± 0.3, n = 8, Female +/+: 4.7 ± 0.3, n = 22, Male +/−: 2.4 ± 0.3, = 18, Female +/−: 3.1 ± 0.3, n = 11; p = 0.13, 2-factor ANOVA. Peak rising dV/dt of AP, combined data from P23–62 constitutive and >P50 conditional heterozygote cases: Male +/+: 584.4 ± 8.8 V/s, n = 48; Female +/+: 588.0 ± 22.8, n = 6; Male +/−: 405.3 ± 8.1, n = 32; Female +/−: 449 ± 19.0, n = 9; p = 0.21, 2-factor ANOVA). Cutting solution contained (in mM): 87 NaCl, 25 $NaHCO_3$, 25 glucose, 75 sucrose, 2.5 KCl, 1.25 NaH_2PO_4, 0.5 $CaCl_2$ and 7 $MgCl_2$; bubbled with 5%CO_2/95%O_2; 4°C. Following cutting, slices were either incubated in the same solution or in the recording solution for 30 min at 33°C, then at room temperature until recording. Recording solution contained (in mM): 125 NaCl, 2.5 KCl, 2 $CaCl_2$, 1 $MgCl_2$, 25 $NaHCO_3$, 1.25 NaH_2PO_4, 25 glucose; bubbled with 5%CO_2/95%O_2; 32–34°C, ~310 mOsm.

Neurons were visualized with differential interference contrast (DIC) optics for conventional visually guided whole-cell recording, or with 2-photon-guided imaging of reporter-driven tdTomato fluorescence overlaid on an image of the slice (scanning DIC). For current-clamp recordings and voltage-clamp recordings of K^+ currents, patch electrodes (Schott 8250 glass, 3–4 MΩ tip resistance) were filled with a solution containing (in mM): 113 K-Gluconate, 9 HEPES, 4.5 $MgCl_2$, 0.1 EGTA, 14 $Tris_2$-phosphocreatine, 4 Na_2-ATP, 0.3 tris-GTP; ~290 mOsm, pH: 7.2–7.25. For Ca^{2+} imaging, EGTA was replaced with 250 μM Fluo-5F and 20 μM Alexa 594. For voltage-clamp recordings of persistent Na+ currents and synaptic activity, internal solution contained (in mM): 110 $CsMeSO_3$, 40 HEPES, 1 KCl, 4 NaCl, 4 Mg-ATP, 10 Na-phosphocreatine, 0.4 Na_2-GTP, 0.1 EGTA; ~290 mOsm, pH: 7.22. All data were corrected for measured junction potentials of 12 and 11 mV in K- and Cs-based internals, respectively.

Electrophysiological data were acquired using Multiclamp 700A or 700B amplifiers (Molecular Devices) via custom routines in IgorPro (Wavemetrics). For measurements of action potential waveform, data were acquired at 50 kHz and filtered at 20 kHz. For all other measurements, data were acquired at 10–20 kHz and filtered at 3–10 kHz. For current-clamp recordings, pipette capacitance was compensated by 50% of the fast capacitance measured under gigaohm seal conditions in voltage-clamp prior to establishing a whole-cell configuration, and the bridge was balanced. For voltage-clamp recordings, pipette capacitance was compensated completely, and series resistance was compensated 50%. Series resistance was <15 MΩ in all recordings. Experiments were omitted if input resistance changed by > ±15%.

Between P4 and P10, whole-cell current-clamp recordings were made from in the center of the cortical plate, corresponding to developing layer 5 (Cánovas et al., 2015). Putative pyramidal cells were identified based on regular spiking characteristics. Pyramidal cell identity was validated by 2-photon visualization of dendritic spines in a subset of these recordings (25/81). After P13, laminae became more distinct and recordings were restricted to L5b. In pyramidal cells aged >P17, AP characteristics are known to vary based cell class (Clarkson et al., 2017; Dembrow et al., 2010). To minimize variability, recordings were restricted to cells with low or high HCN expression levels, corresponding to intratelencephalic (IT) or pyramidal tract (PT) neurons, respectively. In current clamp, PT

neurons were defined as those that exhibited a voltage rebound more depolarized that V_{rest} following a strong hyperpolarizing current (−400 pA, 120 ms) that peaked within 90 ms of current offset (Clarkson et al., 2017). All others were defined as IT. These metrics were not employed in cells from <P15 due to a lack of mature HCN-mediated current. AP threshold and peak dV/dt measurements were determined from the first AP evoked by a near-rheobase current in pyramidal cells (300 ms duration; 10 pA increments), or the first AP within a train of APs with a minimum inter-AP frequency of 25 Hz in inhibitory neurons. Threshold was defined as the V_m when dV/dt measurements first exceeded 15 V/s.

Miniature excitatory and inhibitory postsynaptic currents (mEPSC, mIPSC) were assessed in the presence of 10 μM R-CPP and 400 nM TTX. mEPSCs and mIPSCs were measured while voltage-clamping neurons at −80 and 0 mV, respectively. Events were detected using a deconvolution algorithm based on Pernía-Andrade et al. (Pernía-Andrade et al., 2012), with a noise threshold of 3.5x. All events larger than ±2 pA that were separated by 1 ms were analyzed and subsequently screened manually. Baseline recording noise was not different across genotype (P27 mEPSC root mean square noise, WT: 2.1 ± 0.2 pA, n = 23; *Scn2a*$^{+/-}$: 2.2 ± 0.2 pA, n = 19, p = 0.6, Mann-Whitney test).

In experiments measuring paired pulse ratio and AMPA:NMDA ratio, EPSCs were evoked via a bipolar glass theta electrode placed ~200 μm lateral to the recorded neuron in layer 5. Paired pulse ratio was assessed in the presence of 10 μM R-CPP and 25 μM picrotoxin at −80 mV. Overall divalent concentration was maintained when calcium was lowered from 2 to 1 mM by increasing $MgCl_2$ from 1 to 2 mM. For AMPA:NMDA ratio, R-CPP was omitted and neurons were held at −80 and +30 mV to assess AMPA and NMDA-mediated components. AMPA and NMDA components were defined as the peak inward current at −80 mV and the outward current 50 ms after stimulus onset at +30 mV, respectively.

For sparse Cre expression experiments, mice were anesthetized with isoflurane and positioned in a stereotaxic apparatus. 500 nL volumes of AAV-EF1A-Cre-IRES-mCherry (UNC Vector Core) diluted with saline (1:10) were injected into the mPFC of *Scn2a*$^{fl/+}$ mice (stereotaxic coordinates [mm]: anterior-posterior [AP], +1.7, mediolateral [ML] −0.35; dorsoventral [DV]: −2.6). Mice were used in experiments four weeks post injection.

Persistent Na^+ and currents were activated with 500 ms voltage steps from −90 mV and corrected using p/n leak subtraction. 10–15 trials were averaged per voltage step. Current amplitudes were calculated as the average of the last 100 ms of each step. Experiments were performed in 25 μM picrotoxin, 10 μM NBQX, 10 mM TEA, 2 mM 4-AP, 200 μM Cd^{2+}, 2 μM TTA-P2, and 1 mM Cs^+. K^+ currents were activated with 500 ms voltage steps from −90 to −20, in 10 mV increments. 5 trials were averaged per voltage step. Current amplitudes were calculated from the transient peak and sustained components (last 50 ms). Experiments were performed in 500 nM TTX, 25 μM picrotoxin, 10 μM NBQX, and 1 mM Cs^+. Ca^{2+} channels were not blocked to allow for activation of Ca^{2+}-dependent K^+ channels.

In burst-based spike timing-dependent plasticity protocols, excitatory postsynaptic potentials (EPSPs) were evoked with a theta stimulating electrode placed in layer 1, 25–50 μm from the L1/2 border, 350–500 μm dorsal to the recorded L5b pyramidal cell. After establishing a

stable baseline (EPSP ISI: 0.1 Hz), EPSPs were paired with AP bursts evoked by 500–800 pA somatic current steps (20 ms, onset: 10 ms after EPSP stimulation, 2 APs at >100 Hz). These EPSP-AP pairings were delivered in a train of 5 at 100 ms ISI. Trains were repeated every 5s for 20 trials. Following induction, EPSP stimulation frequency was reset to 0.1 Hz, and changes in EPSP slope were assessed by comparing data 15–25 min following induction to baseline. For experiments performed in 5 nM TTX, bursts were evoked with somatic current injection steps of larger amplitude (800–1500 pA).

Two-photon Imaging: Two-photon laser scanning microscopy (2PLSM) was performed as previously described (Bender and Trussell, 2009). A 2-photon source (Coherent Ultra II) was tuned to 810 nm for morphology and calcium imaging. Epi- and transfluorescence signals were captured either through a 40×, 0.8 NA objective for calcium imaging or a 60×, 1.0 NA objective for spine morphology imaging, paired with a 1.4 NA oil immersion condenser (Olympus). Fluorescence was split into red and green channels using dichroic mirrors and band-pass filters (575 DCXR, ET525/70m-2p, ET620/60m-2p, Chroma). Green fluorescence (Fluo-5F) was captured with 10770–40 photomultiplier tubes selected for high quantum efficiency and low dark counts (PMTs, Hamamatsu). Red fluorescence (Alexa 594) was captured with R9110 PMTs. Data were collected in linescan mode (2–2.4 ms/line, including mirror flyback). For calcium imaging, data were presented as averages of 10–20 events per site, and expressed as $\Delta(G/R)/(G/R)_{max}*100$, where $(G/R)_{max}$ was the maximal fluorescence in saturating Ca^{2+} (2 mM) (Yasuda et al., 2004). Backpropagation experiments were performed in 25 μM picrotoxin, 10 μM NBQX and 10 μM R-CPP.

Spine morphology and density images were obtained during 2PLSM images obtained at 2x the Nyquist resolution limit for 810 nm excitation, with z-stacks through the dendritic arbor (0.1 μm steps in the z-axis). For constitutive knockout animals, z-stacks of dendritic spines were acquired developing (P5–6) and mature (P24–36) neurons from secondary or tertiary dendritic branches in the apical tuft (Mean distance from soma: P24–36 WT = 350 ± 52 μm, P24–36 *Scn2a*$^{+/-}$ = 308 ± 37 μm, P5–6 WT = 197 ± 39 μm, P24–36 *Scn2a*$^{+/-}$ = 197 ± 68 μm) and primary and secondary basal dendritic branches (Mean distance P24–36 WT = 99 ± 23 μm, P24–36 *Scn2a*$^{+/-}$ = 106 ± 25 μm). For conditional knockout animals, z-stacks were acquired from P75–76 *Scn2a*$^{fl/+}$::CaMKII-Cre mice and littermate controls from secondary or tertiary dendritic branches in the apical tuft (WT = 390 ± 51 μm, *Scn2a*$^{fl/+}$::CaMKII-cre = 401 ± 30 μm) and primary and secondary basal dendritic branches (WT = 98 ± 23 μm, *Scn2a*$^{fl/+}$::CaMKII-Cre = 86 ± 25 μm). Stacks were post-processed with the CANDLE denoising protocol (Coupé et al., 2012), then reconstructed using IMARIS 6 (Bitplane). Maximum intensity image projections are displayed within the main and supplemental figures using the “Red Hot” lookup table (FIJI). Full dendritic reconstructions were stitched together using pairwise stitching in FIJI before generation of maximum intensity projection.

Behavioral analyses: Three separate cohorts of mice were assessed, blind to genotype. In the first, tests included open field, elevated plus maze, balance beam, rotarod, nesting, spontaneous alternation, grooming, response and reversal learning, and three trial social Interaction. Based on results of this screen, four trial social preference was assessed in a second cohort and response and reversal learning was assessed in the second and third

cohort. Open field and elevated plus maze were also reassessed in each cohort to determine whether each cohort responded similarly in these anxiety-related assays. Open Field – Mice were transferred to the testing room 60 minutes prior to the start of testing. Mice were then placed in a clear plastic chamber (41 × 41 × 30 cm) and allowed to explore. Movement in the center and outer periphery were recorded by an array of 16 × 16 photobeams (San Diego Instruments).

Elevated plus maze: Mice were placed at the center of an elevated plus maze consisting of two open arms (5.715 cm wide, 70.485 cm long), and two enclosed arms (5.715 cm wide, 70.485 cm long, 16.51cm walls) elevated 63 cm above the ground and were allowed to explore for 10 minutes. Location, distance travelled, and arm entries were measured by infrared photobeam breaks.

Balance beam: On day 1, mice were first trained to talk across a wide beam (37 cm long x 15.875 mm diameter circular beam) over two guided trials. Following training, mice completed three trials (15-minute inter-trial interval) where they were placed end of the beam and traversed the wide beam unguided into an opposing dark chamber. On day 2 the mice completed three trials using a medium beam (37 cm x 12.7 mm diameter circular beam), and on day 3 three trials were completed on the small beam (37 cm x 6.35 mm wide square beam). For each tested trial, the latency to traverse, number of foot slips, and falls were recorded. All testing was performed under normal light conditions.

Rotarod: Mice were trained on a rotarod apparatus over three trials (inter-trial interval 15 minutes) with the rod rotating at a constant speed of 16 rotations per minute (RPM). Following training, mice were tested on 2 consecutive days with 2 sessions of 3 trials each (2-hour inter-session interval, 15-minute inter-trial interval) in which mice were placed on a rotatrod apparatus that gradually accelerated from 4 RPM to 40 RPM in 4 rpm increments every 30 seconds. Trials would end when the mouse would fall off the apparatus or after 5 minutes. All testing was performed under normal light conditions.

Nesting: Mice were placed in a standard mouse cage with 2 cm of paper chip bedding and a single nestlet (5 cm square of pressed cotton batting). Nests in the cage were then scored 2, 6, and 24 hours after the introduction of the mouse on the following scale: 0 = nestlet untouched, 1 = less than 10% of the nestlet is shredded, 2 = 10–50% of the nestlet is shredded but there is no shape to the nest, 3 = 10–50% of the nestlet is shredded and there is shape to the nest, 4 = 50–90% of the nestlet is shredded but there is no shape to the nest, 5 = 50–90% of the nestlet is shredded and there is shape to the nest, 6 = Over 90% of the nestlet is shredded but the nest is flat, 7 = Over 90% of the nestlet is shredded and the nest has walls that are as tall as the mouse on at least 50% of its sides. Half scores were given to nests that lacked well-defined walls but had clear indentations in the middle where the mouse could sit.

Spontaneous Alternation: Mice were placed in an arm of a Y-maze consisting of three arms (30 × 5.5 × 15 cm) and allowed to explore for 6 minutes. Successful alterations were counted when the mouse entered all three arms in succession without repeating an arm.

Percent alternation was calculated by the total number of alterations in 6 minutes/(total number of entries − 2) * 100. Entries were defined as all four paws entering an arm.

Grooming: Mice were placed in a clear plastic container and left undisturbed for 20 minutes. Following 10 minutes of habituation, the number of grooming bouts and the total time spent grooming during the subsequent 10-minute period were then manually scored.

Response and reversal learning: Mice were singly housed and habituated to the testing room for two days prior to the start of testing. Under red light conditions, mice were placed in the start of a water T-maze (10 cm wide, 31 cm long and 17 cm tall) and were required to locate a submerged escape platform at the end of either the right of left arm of the T-maze. Mice performed 4 trials per day in 2 sessions of 2 trials each (3-hour inter-session interval and 15 minute inter-trial interval) for four consecutive days. The platform location remained in the same location across trials for each mouse, and platform location was counterbalanced between mice. On day 5, the platform location was moved to the opposite arm and mice were required to learn the new platform location. Mice performed 6 trials a day in 2 separate sessions of 3 trials (3-hour inter-session interval and 15 minute inter-trial interval) for 4 consecutive days. The maximum length of each trial was 60 seconds, and if mice failed to find the platform within the time limit they were guided to the platform. After successfully finding the platform, the mice were allowed to remain for 10 seconds. Trials were considered incorrect if the mouse entered failed to enter the correct arm first or if the trial time limit expired. All trials were recorded and tracked using Ethovision (Noldus).

Social Approach: Testing was conducted with a white acrylic box divided into two chambers with clear acrylic dividers containing arch-shaped entrances at their center (24in. long, divided into two 12 in chambers, 16 in. wide, and 8.75 in. tall). The chambers contained 10cm square, open-bottomed social enclosures made of clear acrylic with two staggered rows of small access holes (0.5cm in diameter) 2.5cm from the bottom on the 2 sides of the enclosures facing toward the center of the chamber. On day one, mice were first habituated to the empty testing apparatus in 3 10-minute sessions (Mice were returned to their home cage for at least 10 minutes between sessions). On day 2, mice were allowed to explore the empty apparatus for a fourth habituation trial. Social approach was then assessed in a fifth trial by placing a stimulus mouse in one of the two enclosures and the test mouse was allowed to explore either the empty or social enclosures for 10 minutes. Each trial was recorded by video and analyzed with Ethovision. Interaction time was considered the total time spent sniffing within 2 cm of the social enclosures.

Four Trial Social Preference: Sex-matched stimulus mice were habituated to the enclosures for 3 10-minute sessions, between which they were returned to their home cages for at least 10 minutes. Both the experimental and stimulus mice were brought into testing room and given one hour to acclimate to the normal lighting conditions and room prior to testing. For trial 1, the stimulus and toy mouse (Hexbug 480–4466, white) were placed in the enclosures, after which the experimental mouse was placed in the chamber and given 10 minutes to freely explore the box and interact with the social enclosures. The stimulus and experimental mouse were then returned to their home cages for 1 hour before starting trial 2. Trial 2 and 3

proceeded identically to trial 1, using the same stimulus mouse in the same social enclosure. Trial 4 proceeded as in trials 1–3, however the toy mouse was replaced with a novel sex-matched stimulus mouse. For three trial social interaction, only trials 1–3 were assessed. Social preference was assessed on trial 4. Each trial was recorded by video and analyzed with Ethovision. Interaction time was considered the total time spent sniffing within 2 cm of the social enclosures.

Modeling: A pyramidal cell compartmental model was implemented in the NEURON environment (v7.5), with baseline distributions of $Na_V1.2$ and $Na_V1.6$ set as previously described (Ben-Shalom et al., 2017), based on a pyramidal cell model by Hallermann et al. (2012). For phase plane comparisons, the first AP evoked with 2.2 nA stimulus intensity (100 ms duration) were compared in each model configuration. For backpropagation into dendritic arbors, stimuli were shorted to 20 ms to match empirical stimulus conditions (STDP). Stimulus intensity was increased to 2.7 nA. Relative distributions of $Na_V1.2$ and $Na_V1.6$ in the proximal AIS, soma and dendrite were adjusted as described in figure legends. AP waveforms were assessed at 5 locations along the apical dendrite, and AP amplitude was defined as the difference between AP peak V_m and AP threshold (when voltage first exceeds 15 V/s).

Chemicals: Fluo-5F pentapotassium salt, and Alexa Fluor 594 hydrazide Na^+ salt were from Invitrogen. Picrotoxin, R-CPP, and NBQX were from Tocris. TTX-citrate was from Alomone. All others were from Sigma.

Quantification and Statistical Analysis—Data are summarized either as single points with error bars (mean ± standard error) or with box plots depicting the median, quartiles, and 90% tails with individual datapoints overlaid. n denotes cells for all electrophysiology, spines for spine morphology, and animals for behavior. Data were obtained from 2–9 mice per condition for electrophysiology and imaging experiments. Behavioral cohorts were randomized and the experimentalist was blind to genotype. For electrophysiology and imaging experiments, acute slices were typically prepared from WT and conditional or constitutive *Scn2a*$^{+/-}$ littermates simultaneously (genotype blind to experimentalists), with experiments interleaved between the two genotypes to control for recording conditions. Group sample sizes were chosen based on standards in the field, and no statistical methods were used to predetermine sample size. Unless specifically noted, no assumptions were made about the underlying distributions of the data and two-sided, rank-based nonparametric tests were used. Statistical tests are noted throughout text. Significance was set at an alpha value of 0.05, with a Bonferroni correction for multiple comparisons when appropriate. Statistical analysis was performed using Prism 8 (Graphpad Software), Statview (SAS), and custom routines in Matlab R2016b (Mathworks), Python 3.6.4 and R 3.4.3.

Supplementary Material

Refer to Web version on PubMed Central for supplementary material.

Acknowledgments:

We are grateful to Drs. E. Glasscock and M. Montal for providing *Scn2a*$^{+/-}$ mice, and to Drs. G. Davis, K. Kay, D. Manoli, M. Scanziani and members of the Bender and Sanders labs for critically assessing this work. Behavioral data were obtained with the help of Dr. M. Gill and the Gladstone Institutes' Neurobehavioral Core. CaMKII-Cre::Ai14 image acquisition and analysis of dendritic spines was performed at the Gladstone Institutes' Histology & Light Microscopy Core. This research was supported by SFARI grant 513133 (KJB), the Natural Sciences and Engineering Research Council (NSERC) of Canada PGS-D Scholarship (PWES), National Institutes of Health Grant No. F32 NS095580 (RBS) and R01 MH110928 (SJS).

References:

Ariav G, Polsky A, and Schiller J. (2003). Submillisecond precision of the input-output transformation function mediated by fast sodium dendritic spikes in basal dendrites of CA1 pyramidal neurons. J. Neurosci 23, 7750–7758. [PubMed: 12944503]

Barth AMI, Vizi ES, Zelles T, and Lendvai B. (2008). α_2 -Adrenergic Receptors Modify Dendritic Spike Generation Via HCN Channels in the Prefrontal Cortex. J. Neurophysiol 99, 394–401. [PubMed: 18003878]

Bateup HS, Takasaki KT, Saulnier JL, Denefrio CL, and Sabatini BL (2011). Loss of Tsc1 in vivo impairs hippocampal mGluR-LTD and increases excitatory synaptic function. J. Neurosci 31, 8862–8869. [PubMed: 21677170]

Bean BP (2007). The action potential in mammalian central neurons. Nat. Rev. Neurosci 8, 451–465. [PubMed: 17514198]

Beaulieu-Laroche L, and Harnett MT (2018). Dendritic Spines Prevent Synaptic Voltage Clamp. Neuron 97, 75–82.e3.

Begemann A, Acuña MA, Zweier M, Vincent M, Steindl K, Bachmann-Gagescu R, Hackenberg A, Abela L, Plecko B, Kroell-Seger J, et al. (2019). Further corroboration of distinct functional features in SCN2A variants causing intellectual disability or epileptic phenotypes. Mol. Med 25, 6. [PubMed: 30813884]

Ben-Shalom R, Keeshen CM, Berrios KN, An JY, Sanders SJ, and Bender KJ (2017). Opposing Effects on Na V 1.2 Function Underlie Differences Between SCN2A Variants Observed in Individuals With Autism Spectrum Disorder or Infantile Seizures. Biol. Psychiatry 82, 224–232. [PubMed: 28256214]

Bender KJ, and Trussell LO (2009). Axon Initial Segment Ca2+ Channels Influence Action Potential Generation and Timing. Neuron 61, 259–271. [PubMed: 19186168]

Bender KJ, and Trussell LO (2012). The physiology of the axon initial segment. Annu Rev Neurosci 35, 249–265. [PubMed: 22443507]

Bourgeron T. (2015). From the genetic architecture to synaptic plasticity in autism spectrum disorder. Nat. Rev. Neurosci 16, 551–563. [PubMed: 26289574]

Bozdagi O, Sakurai T, Papapetrou D, Wang X, Dickstein DL, Takahashi N, Kajiwara Y, Yang M, Katz AM, Scattoni M, et al. (2010). Haploinsufficiency of the autism-associated Shank3 gene leads to deficits in synaptic function, social interaction, and social communication. Mol. Autism 1, 15. [PubMed: 21167025]

Brunner D, Kabitzke P, He D, Cox K, Thiede L, Hanania T, Sabath E, Alexandrov V, Saxe M, Peles E, et al. (2015). Comprehensive Analysis of the 16p11.2 Deletion and Null Cntnap2 Mouse Models of Autism Spectrum Disorder. PLoS One 10, e0134572.

Cánovas J, Berndt FA, Sepúlveda H, Aguilar R, Veloso FA, Montecino M, Oliva C, Maass JC, Sierralta J, and Kukuljan M. (2015). The Specification of Cortical Subcerebral Projection Neurons Depends on the Direct Repression of TBR1 by CTIP1/BCL11a. J. Neurosci 35, 7552–7564. [PubMed: 25972180]

Chadman KK, Gong S, Scattoni ML, Boltuck SE, Gandhy SU, Heintz N, and Crawley JN (2008). Minimal aberrant behavioral phenotypes of neuroligin-3 R451C knockin mice. Autism Res. 1, 147–158. [PubMed: 19360662]

Clarkson RL, Liptak AT, Gee SM, Sohal VS, and Bender KJ (2017). D3 Receptors Regulate Excitability in a Unique Class of Prefrontal Pyramidal Cells. J. Neurosci 37, 5846–5860. [PubMed: 28522735]

Contractor A, Klyachko VA, and Portera-Cailliau C. (2015). Altered Neuronal and Circuit Excitability in Fragile X Syndrome. Neuron 87, 699–715. [PubMed: 26291156]

Coupé P, Munz M, Manjón JV, Ruthazer ES, and Collins DL (2012). A CANDLE for a deeper in vivo insight. Med. Image Anal 16, 849–864. [PubMed: 22341767]

Darnell JC, Van Driesche SJ, Zhang C, Hung KYS, Mele A, Fraser CE, Stone EF, Chen C, Fak JJ, Chi SW, et al. (2011). FMRP Stalls Ribosomal Translocation on mRNAs Linked to Synaptic Function and Autism. Cell 146, 247–261. [PubMed: 21784246]

Dembrow NC, Chitwood RA, and Johnston D. (2010). Projection-Specific Neuromodulation of Medial Prefrontal Cortex Neurons. J. Neurosci 30, 16922–16937.

Dobi A, Seabold GK, Christensen CH, Bock R, and Alvarez VA (2011). Cocaine-induced plasticity in the nucleus accumbens is cell specific and develops without prolonged withdrawal. J. Neurosci 31, 1895–1904. [PubMed: 21289199]

Ey E, Yang M, Katz AM, Woldeyohannes L, Silverman JL, Leblond CS, Faure P, Torquet N, Le Sourd A-M, Bourgeron T, et al. (2012). Absence of deficits in social behaviors and ultrasonic vocalizations in later generations of mice lacking neuroligin4. Genes, Brain Behav. 11, n/a-n/a.

Favero M, Sotuyo NP, Lopez E, Kearney JA, and Goldberg EM (2018). A Transient Developmental Window of Fast-Spiking Interneuron Dysfunction in a Mouse Model of Dravet Syndrome. J. Neurosci 38, 7912–7927. [PubMed: 30104343]

Feldman DE (2012). The Spike-Timing Dependence of Plasticity. Neuron 75, 556–571. [PubMed: 22920249]

Gazina EV, Leaw BTW, Richards KL, Wimmer VC, Kim TH, Aumann TD, Featherby TJ, Churilov L, Hammond VE, Reid CA, et al. (2015). 'Neonatal' Nav1.2 reduces neuronal excitability and affects seizure susceptibility and behaviour. Hum. Mol. Genet 24, 1457–1468. [PubMed: 25378553]

Gee S, Ellwood I, Patel T, Luongo F, Deisseroth K, and Sohal VS (2012). Synaptic Activity Unmasks Dopamine D2 Receptor Modulation of a Specific Class of Layer V Pyramidal Neurons in Prefrontal Cortex. J. Neurosci 32, 4959–4971. [PubMed: 22492051]

Geisheker MR, Heymann G, Wang T, Coe BP, Turner TN, Stessman HAF, Hoekzema K, Kvarnung M, Shaw M, Friend K, et al. (2017). Hotspots of missense mutation identify neurodevelopmental disorder genes and functional domains. Nat. Neurosci 20, 1043–1051. [PubMed: 28628100]

Golden CEM, Breen MS, Koro L, Sonar S, Niblo K, Browne A, Burlant N, Di Marino D, De Rubeis S, Baxter MG, et al. (2019). Deletion of the KH1 Domain of Fmr1 Leads to Transcriptional Alterations and Attentional Deficits in Rats. Cereb. Cortex

Golding NL, Staff NP, and Spruston N. (2002). Dendritic spikes as a mechanism for cooperative long-term potentiation. Nature 418, 326–331. [PubMed: 12124625]

Gong B, Rhodes KJ, Bekele-Arcuri Z, and Trimmer JS (1999). Type I and type II Na+ channel ?-subunit polypeptides exhibit distinct spatial and temporal patterning, and association with auxiliary subunits in rat brain. J. Comp. Neurol 412, 342–352. [PubMed: 10441760]

Greer PL, Hanayama R, Bloodgood BL, Mardinly AR, Lipton DM, Flavell SW, Kim T-K, Griffith EC, Waldon Z, Maehr R, et al. (2010). The Angelman Syndrome Protein Ube3A Regulates Synapse Development by Ubiquitinating Arc. Cell 140, 704–716. [PubMed: 20211139]

Gulledge AT, and Stuart GJ (2003). Action potential initiation and propagation in layer 5 pyramidal neurons of the rat prefrontal cortex: absence of dopamine modulation. J. Neurosci 23, 11363–11372.

Hallermann S, de Kock CPJ, Stuart GJ, and Kole MHP (2012). State and location dependence of action potential metabolic cost in cortical pyramidal neurons. Nat. Neurosci 15, 1007–1014. [PubMed: 22660478]

Hanse E, Seth H, and Riebe I. (2013). AMPA-silent synapses in brain development and pathology. Nat. Rev. Neurosci 14, 839–850. [PubMed: 24201185]

Hu W, and Bean BP (2018). Differential Control of Axonal and Somatic Resting Potential by Voltage-Dependent Conductances in Cortical Layer 5 Pyramidal Neurons. Neuron 97, 1315–1326.e3.

Hu W, Tian C, Li T, Yang M, Hou H, and Shu Y. (2009). Distinct contributions of Na(v)1.6 and Na(v)1.2 in action potential initiation and backpropagation. Nat. Neurosci 12, 996–1002. [PubMed: 19633666]

Johnson KW, Herold KF, Milner TA, Hemmings HC, and Platholi J. (2017). Sodium channel subtypes are differentially localized to pre- and post-synaptic sites in rat hippocampus. J. Comp. Neurol 525, 3563–3578. [PubMed: 28758202]

Kampa BM, Letzkus JJ, and Stuart GJ (2006). Requirement of dendritic calcium spikes for induction of spike-timing-dependent synaptic plasticity. J. Physiol 574, 283–290. [PubMed: 16675489]

Kampa BM, Letzkus JJ, and Stuart GJ (2007). Dendritic mechanisms controlling spike-timing-dependent synaptic plasticity. Trends Neurosci. 30, 456–463. [PubMed: 17765330]

Kerchner GA, and Nicoll RA (2008). Silent synapses and the emergence of a postsynaptic mechanism for LTP. Nat. Rev. Neurosci 9, 813–825. [PubMed: 18854855]

Kim Y, Hsu C-L, Cembrowski MS, Mensh BD, and Spruston N. (2015). Dendritic sodium spikes are required for long-term potentiation at distal synapses on hippocampal pyramidal neurons. Elife 4.

Kole MHP, and Stuart GJ (2012). Signal Processing in the Axon Initial Segment. Neuron 73, 235–247. [PubMed: 22284179]

Larkum ME, Zhu JJ, and Sakmann B. (1999a). A new cellular mechanism for coupling inputs arriving at different cortical layers. Nature 398, 338–341. [PubMed: 10192334]

Larkum ME, Kaiser KM, and Sakmann B. (1999b). Calcium electrogenesis in distal apical dendrites of layer 5 pyramidal cells at a critical frequency of back-propagating action potentials. Proc. Natl. Acad. Sci. U. S. A 96, 14600–14604.

Li T, Tian C, Scalmani P, Frassoni C, Mantegazza M, Wang Y, Yang M, Wu S, and Shu Y. (2014). Action Potential Initiation in Neocortical Inhibitory Interneurons. PLoS Biol. 12, e1001944.

Liao Y, Deprez L, Maljevic S, Pitsch J, Claes L, Hristova D, Jordanova A, Ala-Mello S, Bellan-Koch A, Blazevic D, et al. (2010). Molecular correlates of age-dependent seizures in an inherited neonatal-infantile epilepsy. Brain 133, 1403–1414. [PubMed: 20371507]

Lorincz A, and Nusser Z. (2008). Cell-type-dependent molecular composition of the axon initial segment. J. Neurosci 28, 14329–14340.

Lorincz A, and Nusser Z. (2010). Molecular Identity of Dendritic Voltage-Gated Sodium Channels. Science (80-.). 328, 906–909.

Magee JC, and Johnston D. (1997). A synaptically controlled, associative signal for Hebbian plasticity in hippocampal neurons. Science 275, 209–213. [PubMed: 8985013]

Markram H, Lübke J, Frotscher M, and Sakmann B. (1997). Regulation of synaptic efficacy by coincidence of postsynaptic APs and EPSPs. Science 275, 213–215. [PubMed: 8985014]

Markram H, Gerstner W, and Sjöström PJ (2012). Spike-Timing-Dependent Plasticity: A Comprehensive Overview. Front. Synaptic Neurosci 4, 2. [PubMed: 22807913]

Meredith RM, and Mansvelder HD (2010). STDP and Mental Retardation: Dysregulation of Dendritic Excitability in Fragile X Syndrome. Front. Synaptic Neurosci 2, 10. [PubMed: 21423496]

Middleton SJ, Kneller EM, Chen S, Ogiwara I, Montal M, Yamakawa K, and McHugh TJ (2018). Altered hippocampal replay is associated with memory impairment in mice heterozygous for the Scn2a gene. Nat. Neurosci

Mishra V, Karumuri BK, Gautier NM, Liu R, Hutson TN, Vanhoof-Villalba SL, Vlachos I, Iasemidis L, and Glasscock E. (2017). Scn2a deletion improves survival and brain-heart dynamics in the Kcna1-null mouse model of sudden unexpected death in epilepsy (SUDEP). Hum. Mol. Genet 26, 2091–2103. [PubMed: 28334922]

Monteiro P, and Feng G. (2017). SHANK proteins: roles at the synapse and in autism spectrum disorder. Nat. Rev. Neurosci 18, 147–157. [PubMed: 28179641]

Nestor MW, and Hoffman DA (2012). Aberrant dendritic excitability: a common pathophysiology in CNS disorders affecting memory? Mol. Neurobiol 45, 478–487. [PubMed: 22528602]

Ogiwara I, Miyamoto H, Morita N, Atapour N, Mazaki E, Inoue I, Takeuchi T, Itohara S, Yanagawa Y, Obata K, et al. (2007). Nav1.1 localizes to axons of parvalbumin-positive inhibitory interneurons: a circuit basis for epileptic seizures in mice carrying an Scn1a gene mutation. J. Neurosci 27, 5903–5914. [PubMed: 17537961]

Ogiwara I, Miyamoto H, Tatsukawa T, Yamagata T, Nakayama T, Atapour N, Miura E, Mazaki E, Ernst SJ, Cao D, et al. (2018). Nav1.2 haplodeficiency in excitatory neurons causes absence-like seizures in mice. Commun. Biol 1, 96. [PubMed: 30175250]

Pasciuto E, Borrie SC, Kanellopoulos AK, Santos AR, Cappuyns E, D'Andrea L, Pacini L, and Bagni C. (2015). Autism Spectrum Disorders: Translating human deficits into mouse behavior. Neurobiol. Learn. Mem 124, 71–87. [PubMed: 26220900]

Pernía-Andrade AJ, Goswami SP, Stickler Y, Fröbe U, Schlögl A, and Jonas P. (2012). A deconvolution-based method with high sensitivity and temporal resolution for detection of spontaneous synaptic currents in vitro and in vivo. Biophys. J 103, 1429–1439. [PubMed: 23062335]

Planells-Cases R, Caprini M, Zhang J, Rockenstein EM, Rivera RR, Murre C, Masliah E, and Montal M. (2000). Neuronal Death and Perinatal Lethality in Voltage-Gated Sodium Channel αII-Deficient Mice. Biophys. J 78, 2878–2891. [PubMed: 10827969]

De Rubeis S, He X, Goldberg AP, Poultney CS, Samocha K, Ercument Cicek A, Kou Y, Liu L, Fromer M, Walker S, et al. (2014). Synaptic, transcriptional and chromatin genes disrupted in autism. Nature 515, 209–215. [PubMed: 25363760]

Sala C, Futai K, Yamamoto K, Worley PF, Hayashi Y, and Sheng M. (2003). Inhibition of dendritic spine morphogenesis and synaptic transmission by activity-inducible protein Homer1a. J. Neurosci 23, 6327–6337. [PubMed: 12867517]

Sanders SJ (2015). First glimpses of the neurobiology of autism spectrum disorder. Curr. Opin. Genet. Dev 33, 80–92. [PubMed: 26547130]

Sanders SJ, Murtha MT, Gupta AR, Murdoch JD, Raubeson MJ, Willsey AJ, Ercan-Sencicek AG, DiLullo NM, Parikshak NN, Stein JL, et al. (2012). De novo mutations revealed by whole-exome sequencing are strongly associated with autism. Nature 485, 237–241. [PubMed: 22495306]

Sanders SJ, He X, Willsey AJ, Ercan-Sencicek AG, Samocha KE, Cicek AE, Murtha MT, Bal VH, Bishop SL, Dong S, et al. (2015). Insights into Autism Spectrum Disorder Genomic Architecture and Biology from 71 Risk Loci. Neuron 87, 1215–1233. [PubMed: 26402605]

Sanders SJ, Campbell AJ, Cottrell JR, Moller RS, Wagner FF, Auldridge AL, Bernier RA, Catterall WA, Chung WK, Empfield JR, et al. (2018). Progress in Understanding and Treating SCN2A -Mediated Disorders. Trends Neurosci. 0.

Satterstrom FK, Kosmicki JA, Wang J, Breen MS, Rubeis S De, An J-Y,Peng M, Collins RL, Grove J, Klei L, et al. (2018). Novel genes for autism implicate both excitatory and inhibitory cell lineages in risk. BioRxiv 484113.

Shen H, Gipson CD, Huits M, and Kalivas PW (2014). Prelimbic Cortex and Ventral Tegmental Area Modulate Synaptic Plasticity Differentially in Nucleus Accumbens During Cocaine-Reinstated Drug Seeking. Neuropsychopharmacology 39, 1169–1177. [PubMed: 24232172]

Short SM, Oikonomou KD, Zhou W-L, Acker CD, Popovic MA, Zecevic D, and Antic SD (2017). The stochastic nature of action potential backpropagation in apical tuft dendrites. J. Neurophysiol 118, 1394–1414. [PubMed: 28566465]

Silverman JL, Yang M, Lord C, and Crawley JN (2010). Behavioural phenotyping assays for mouse models of autism. Nat. Rev. Neurosci 11, 490–502. [PubMed: 20559336]

Spencer CM, Alekseyenko O, Hamilton SM, Thomas AM, Serysheva E, Yuva-Paylor LA, and Paylor R. (2011). Modifying behavioral phenotypes in Fmr1KO mice: genetic background differences reveal autistic-like responses. Autism Res. 4, 40–56. [PubMed: 21268289]

Stuart GJ, and Häusser M. (2001). Dendritic coincidence detection of EPSPs and action potentials. Nat. Neurosci 4, 63–71. [PubMed: 11135646]

Stuart G, Schiller J, and Sakmann B. (1997). Action potential initiation and propagation in rat neocortical pyramidal neurons. J. Physiol 505 (Pt 3), 617–632. [PubMed: 9457640]

Sugathan A, Biagioli M, Golzio C, Erdin S, Blumenthal I, Manavalan P, Ragavendran A, Brand H, Lucente D, Miles J, et al. (2014). CHD8 regulates neurodevelopmental pathways associated with autism spectrum disorder in neural progenitors. Proc. Natl. Acad. Sci 111, E4468–E4477.

Taddese A, and Bean BP (2002). Subthreshold sodium current from rapidly inactivating sodium channels drives spontaneous firing of tuberomammillary neurons. Neuron 33, 587–600. [PubMed: 11856532]

Tai C, Abe Y, Westenbroek RE, Scheuer T, and Catterall WA (2014). Impaired excitability of somatostatin- and parvalbumin-expressing cortical interneurons in a mouse model of Dravet syndrome. Proc. Natl. Acad. Sci. U. S. A 111, E3139–48.

Tatsukawa T, Raveau M, Ogiwara I, Hattori S, Miyamoto H, Mazaki E, Itohara S, Miyakawa T, Montal M, and Yamakawa K. (2019). Scn2a haploinsufficient mice display a spectrum of phenotypes affecting anxiety, sociability, memory flexibility and ampakine CX516 rescues their hyperactivity. Mol. Autism 10, 15. [PubMed: 30962870]

Tsai N-P, Wilkerson JR, Guo W, Maksimova MA, DeMartino GN, Cowan CW, and Huber KM (2012). Multiple autism-linked genes mediate synapse elimination via proteasomal degradation of a synaptic scaffold PSD-95. Cell 151, 1581–1594. [PubMed: 23260144]

Tzounopoulos T, Kim Y, Oertel D, and Trussell LO (2004). Cell-specific, spike timing–dependent plasticities in the dorsal cochlear nucleus. Nat. Neurosci 7, 719–725. [PubMed: 15208632]

Williams SR, and Mitchell SJ (2008). Direct measurement of somatic voltage clamp errors in central neurons. Nat. Neurosci 11, 790–798. [PubMed: 18552844]

Williams MR, DeSpenza T, Li M, Gulledge AT, and Luikart BW (2015). Hyperactivity of newborn Pten knock-out neurons results from increased excitatory synaptic drive. J. Neurosci 35, 943–959. [PubMed: 25609613]

Willsey AJ, Sanders SJ, Li M, Dong S, Tebbenkamp AT, Muhle RA, Reilly SK, Lin L, Fertuzinhos S, Miller JA, et al. (2013). Coexpression networks implicate human midfetal deep cortical projection neurons in the pathogenesis of autism. Cell 155, 997–1007. [PubMed: 24267886]

Wolff M, Johannesen KM, Hedrich UBS, Masnada S, Rubboli G, Gardella E, Lesca G, Ville D, Milh M, Villard L, et al. (2017). Genetic and phenotypic heterogeneity suggest therapeutic implications in SCN2A-related disorders. Brain 140, 1316–1336. [PubMed: 28379373]

Workman AD, Charvet CJ, Clancy B, Darlington RB, and Finlay BL (2013). Modeling transformations of neurodevelopmental sequences across mammalian species. J. Neurosci 33, 7368–7383. [PubMed: 23616543]

Xu B, Zang K, Ruff NL, Zhang YA, McConnell SK, Stryker MP, and Reichardt LF (2000). Cortical degeneration in the absence of neurotrophin signaling: dendritic retraction and neuronal loss after removal of the receptor TrkB. Neuron 26, 233–245. [PubMed: 10798407]

Xu N, Harnett MT, Williams SR, Huber D, O'Connor DH, Svoboda K, and Magee JC (2012). Nonlinear dendritic integration of sensory and motor input during an active sensing task. Nature 492, 247–251. [PubMed: 23143335]

Yamagata T, Ogiwara I, Mazaki E, Yanagawa Y, and Yamakawa K. (2017). Nav1.2 is expressed in caudal ganglionic eminence-derived disinhibitory interneurons: Mutually exclusive distributions of Nav1.1 and Nav1.2. Biochem. Biophys. Res. Commun 491, 1070–1076. [PubMed: 28784306]

Yashiro K, Riday TT, Condon KH, Roberts AC, Bernardo DR, Prakash R, Weinberg RJ, Ehlers MD, and Philpot BD (2009). Ube3a is required for experience-dependent maturation of the neocortex. Nat. Neurosci 12, 777–783. [PubMed: 19430469]

Yasuda R, Nimchinsky EA, Scheuss V, Pologruto TA, Oertner TG, Sabatini BL, and Svoboda K. (2004). Imaging Calcium Concentration Dynamics in Small Neuronal Compartments. Sci. Signal. 2004, pl5–pl5.

Yi F, Danko T, Botelho SC, Patzke C, Pak C, Wernig M, and Südhof TC (2016). Autism-associated SHANK3 haploinsufficiency causes Ih channelopathy in human neurons. Science 352, aaf2669.

Highlights

- Protein truncation in *SCN2A*/$Na_V1.2$ bears considerable autism spectrum disorder risk
- $Na_V1.2$ governs action potential initiation in immature neocortical pyramidal cells
- Mature *Scn2a*$^{+/-}$ neurons have impaired dendritic excitability and excitatory synapses
- Cell-autonomous loss of $Na_V1.2$ in mature cells alone impairs synaptic function

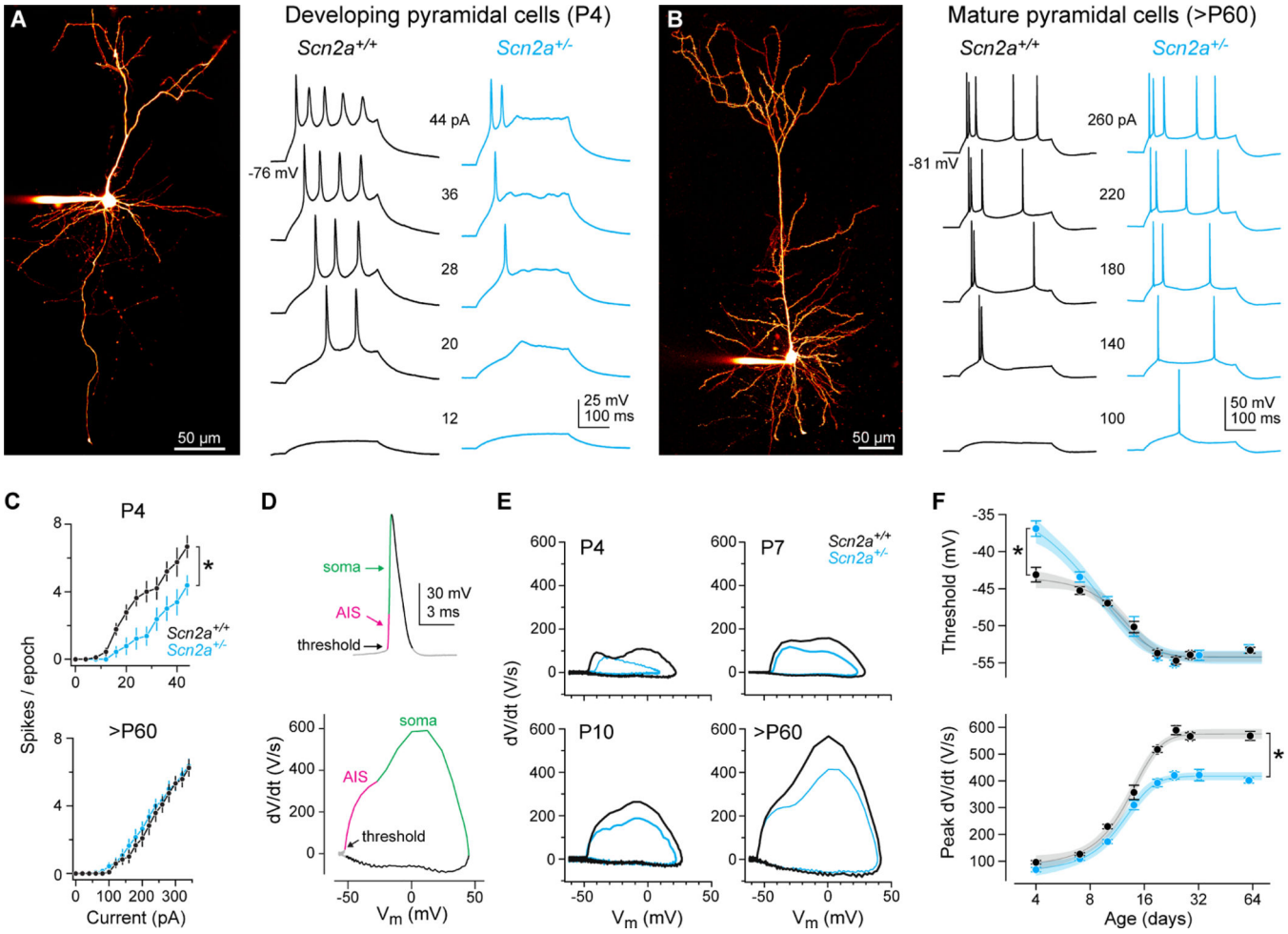

Figure 1: *Scn2a* haploinsufficiency impairs different aspects of neuronal excitability across developmental periods

A: Left, 2-photon laser scanning microscopy (2PLSM) z-stack of developing pyramidal cell (P7). Right, APs generated by current injection (12–44 pA, 300 ms) in $Scn2a^{+/+}$ (black) and $Scn2a^{+/-}$ (cyan) cells. AP data from neurons recorded at P4.

B: Left, 2-photon z-stack of mature thick-tufted pyramidal cell. Right, AP response as in (A).

C: APs (spikes) per 300 ms stimulation epoch for each current amplitude. At P4, $Scn2a^{+/-}$ are less excitable (Firing rate slope between 4–44 pA, $Scn2a^{+/+}$: 0.67 ± 0.07 APs/pA*s, n = 9 cells; $Scn2a^{+/-}$: 0.41 ± 0.07, n = 9 cells, *: p = 0.02, Mann-Whitney). At >P60, no differences are observed between $Scn2a^{+/+}$ and $Scn2a^{+/-}$ cells (Slope between 50–350 pA: $Scn2a^{+/+}$: 0.08 ± 0.007 APs/pA*s, n = 12 cells; $Scn2a^{+/-}$: 0.08 ± 0.005, n = 14 cells, p = 0.96, Mann-Whitney).

D: An AP is plotted as voltage vs. time (top) and dV/dt vs voltage (phase-plane plot, bottom). Different phases of the AP are color-coded across panels to indicated different phases of the AP corresponding to initiation of AP in AIS and full detonation of AP in soma.

E: Phase-plane plots at P4, P7, P10, and >P60 in $Scn2a^{+/+}$ and $Scn2a^{+/-}$ cells. Note recovery of AP threshold (kink) deficit between P4 and P10, and decrements in peak dV/dt that become more pronounced with age.

F: Top: AP threshold across development from P4–64 (log_2 scale for age) in *Scn2a*$^{+/+}$ (black) and *Scn2a*$^{+/-}$ (cyan) mice. Bottom: Peak rising phase dV/dt vs. age. Circles and bars are mean ± SEM within an age group (n = 7–28 cells per group). Data fit with a generalized logistic function with 95% confidence intervals determined from fits to single cells. *: difference in parameters of the sigmoid fits. Top: Left asymptote, *Scn2a*$^{+/+}$: −44.1 ± 0.6 mV, *Scn2a*$^{+/-}$ −35.6 ± 1.6, $p < 0.001$, unpaired t-test. Bottom: Right asymptote, *Scn2a*$^{+/+}$: 587.8 ± 10.2 V/s, *Scn2a*$^{+/-}$: 420.3 ± 9.5, $p < 0.001$, unpaired t-test.

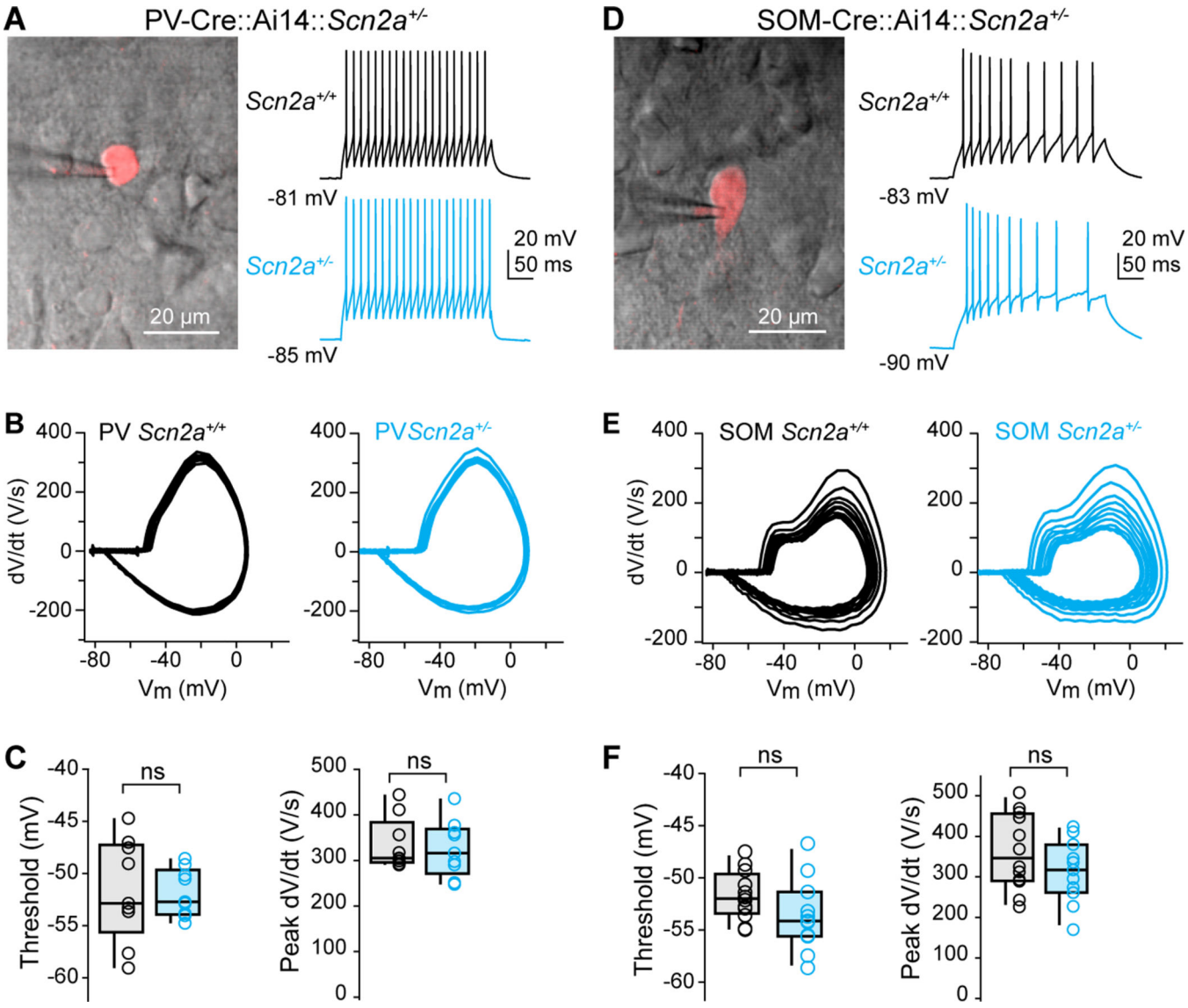

Figure 2: Layer 5 parvalbumin and somatostatin neuron APs are not altered in *Scn2a*$^{+/-}$ mice.

A: 2PLSM single optical section of tdTomato-positive parvalbumin-positive interneuron, overlaid with scanning-DIC image showing pipette in cell-attached configuration. Scale bar: 20 µm.

B: Spiking generated from parvalbumin positive cells in *Scn2a*$^{+/+}$ and *Scn2a*$^{+/-}$ mice.

C: Phase-plane plots of data shown in (B).

D: AP threshold and peak rising dV/dt for the first AP of spike train. Open circles are single cells. Box plots are median, quartiles, and 90% tails. No statistical differences noted. Data obtained from P34–40 animals.

E-H: Identical to A-D, but for somatostatin-positive interneurons. Data obtained from P37–38 animals.

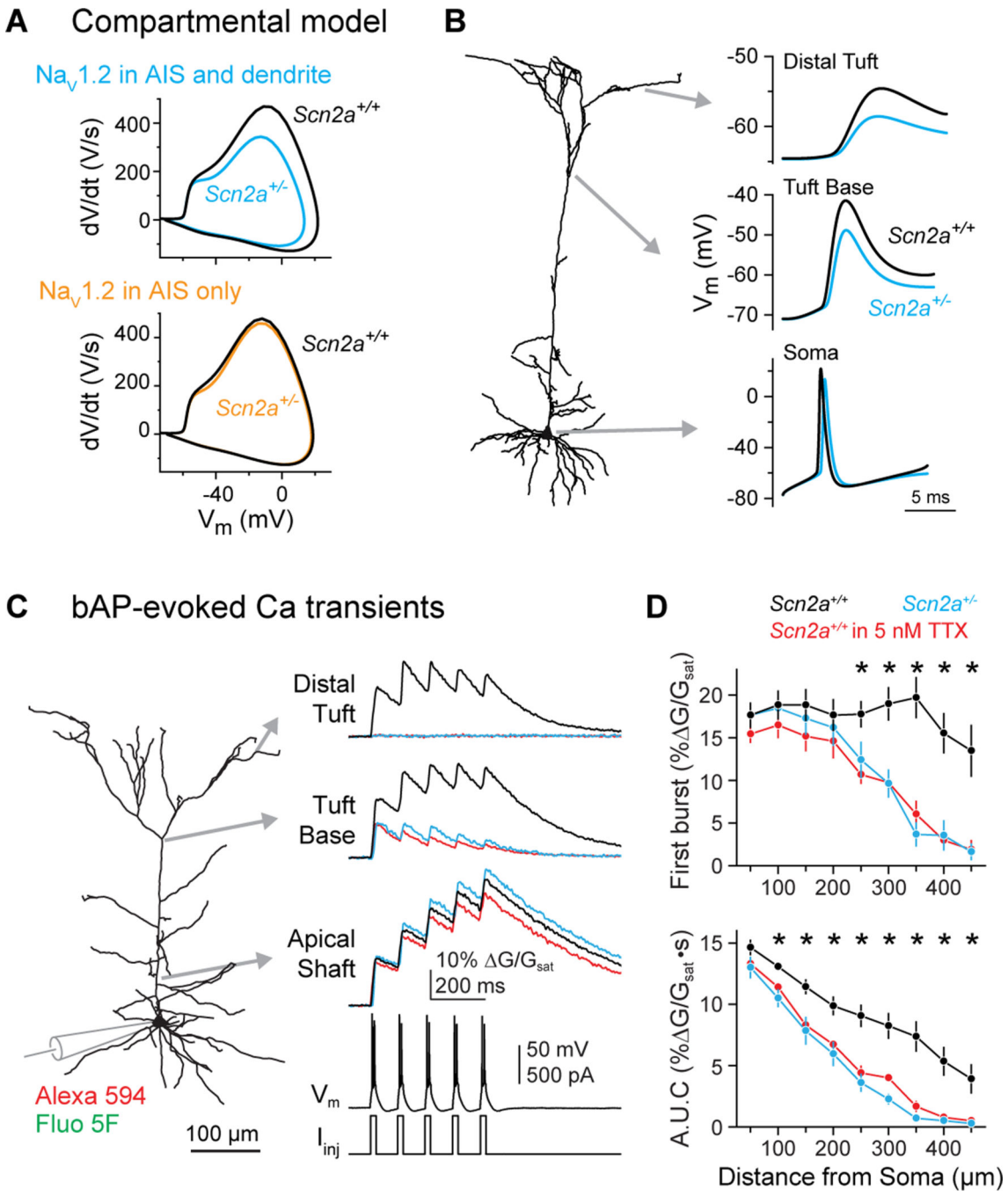

Figure 3: *Scn2a* haploinsufficiency impairs dendritic backpropagation of APs

A: Compartmental model of cortical layer 5 pyramidal cell with two distributions of $Na_V1.2$ and $Na_V1.6$ (see Fig. S5 for other model configurations). Top model has $Na_V1.2$ in the proximal AIS, $Na_V1.6$ in the distal AIS, and $Na_V1.2$ and 1.6 equally co-expressed in the somatodendritic compartment. Note reduction in peak rising dV/dt. Bottom model has $Na_V1.2$ in the proximal AIS only, with $Na_V1.6$ in the somatodendritic and distal AIS compartments. Removal of half the $Na_V1.2$ channels results in only minor changes to AP phase-plane.

B: A single AP evoked in the top model in (A), backpropagating throughout dendrite. More marked differences in AP shape observed in more distal dendritic locations.

C: 2PLSM calcium imaging throughout apical dendrite of L5 thick-tufted neuron. Calcium transients evoked by bursts of AP doublets.

D: Transient amplitude is plotted for the first of 5 bursts (top) and area under the curve from stimulus onset to stimulus offset +100 ms (bottom) in *Scn2a*$^{+/+}$ (n = 10), *Scn2a*$^{+/-}$ (n = 8 cells), and *Scn2a*$^{+/+}$ cells treated with 5 nM TTX (n = 5). Circles and bars are means ± SEM. *: $p < 0.05$, Kruskal-Wallis test.

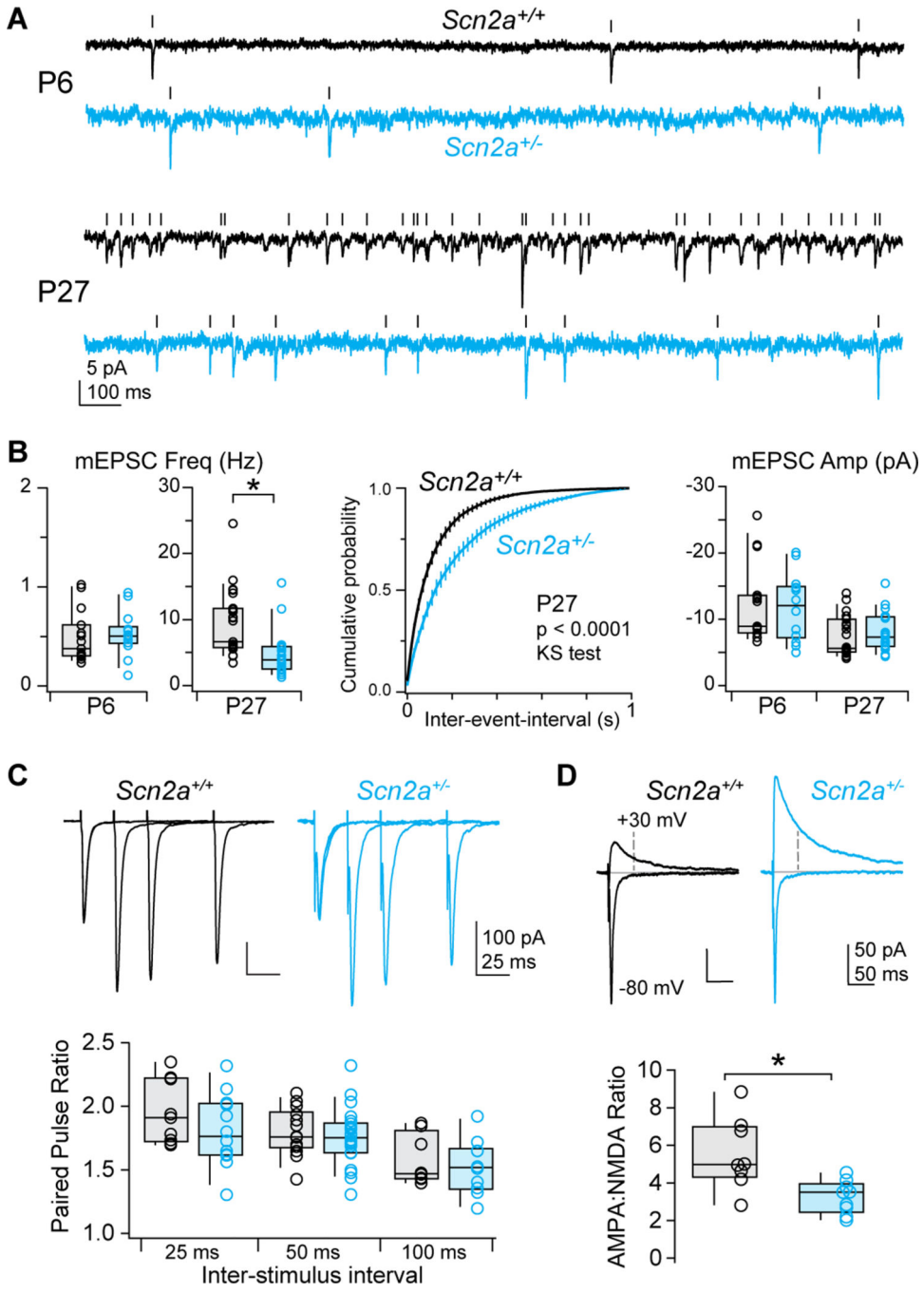

Figure 4: *Scn2a* haploinsufficiency disrupts excitatory synapse function

A: mEPSCs recorded in *Scn2a*$^{+/+}$ (black) and *Scn2a*$^{+/-}$ (cyan) pyramidal cells at P6 and P27. Tick marks denote detected events.

B: Left, average mEPSC frequency per cell (open circles). Box plots are median, quartiles, and 90% tails. Note that frequency range is different for P6 and P27. Middle, cumulative probability distribution of mEPSC event intervals at P27. Distributions were generated per cell, then averaged. Bars are SEM. $p < 0.0001$, Kolmogorov-Smirnov test. Right, average mEPSC amplitude per cell.

C: Paired pulse ratio of evoked excitatory inputs to *Scn2a*$^{+/+}$ (black) and *Scn2a*$^{+/-}$ (cyan) pyramidal cells at 3 different stimulus intervals. Bottom, summary grouped by inter-stimulus interval. No differences noted.

D: Top, AMPA receptor-mediated and mixed AMPA/NMDA receptor-mediated evoked EPSCs at −80 and +30 mV, respectively. Dashed line denotes time at which NMDA receptor-mediated component was calculated. Bottom, AMPA-NMDA ratio in *Scn2a*$^{+/+}$ and *Scn2a*$^{+/-}$ neurons. * $p < 0.01$, Mann-Whitney.

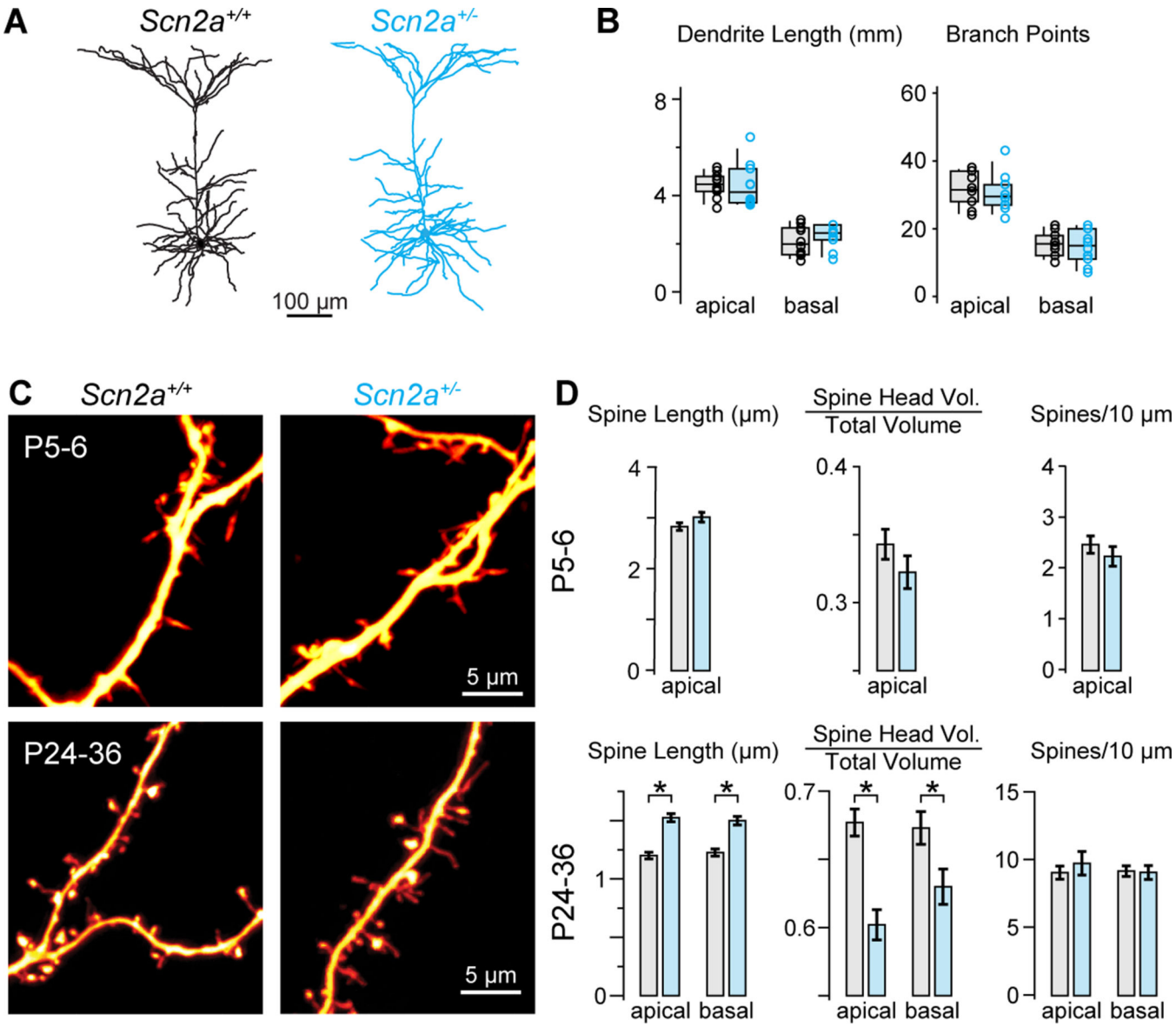

Figure 5: Dendritic spines are morphologically immature in *Scn2a*$^{+/-}$ cells

A: Examples of dendritic morphology in P22–25 *Scn2a*$^{+/+}$ (black) and *Scn2a*$^{+/-}$ (cyan) pyramidal cells.

B: Overall dendrite length and branch points in apical and basal trees. Open circles are single cells. Box plots are median, quartiles, and 90% tails. (*Scn2a*$^{+/+}$: n = 10 cells; *Scn2a*$^{+/-}$: n = 10 cells). No differences across genotype noted.

C: Examples of spines along apical dendrites of immature (P5–6) and more mature (P24–36) neurons.

D: Overall spine length from shaft to spine head, volume of spine head relative to total volume of head and shaft, and number of spines per length of dendrite were measured in apical dendrites of P5–6 neurons (n = 560–685 spines per group, 1–4 dendritic branches per cells, 10 cells per group; note that basal dendrites often lacked spines at this age and were therefore not assessed). Spines along both apical and basal dendrites were imaged in P24–36

neurons (n = 500–600 spines per group, 1–3 dendritic branches per cell, 6 cells per group). *: $p < 0.05$, Mann-Whitney.

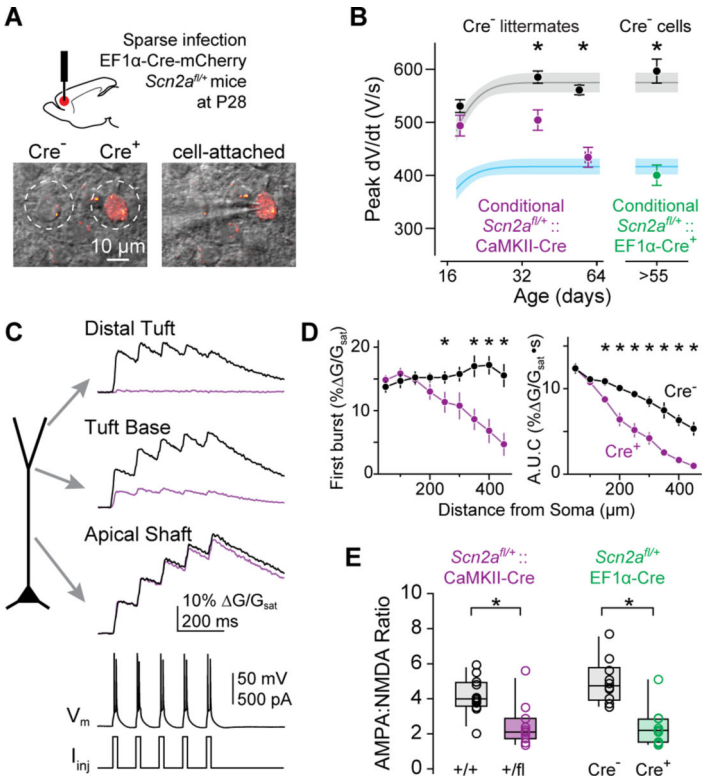

Figure 6: Inducing *Scn2a* haploinsufficiency late in development disrupts dendritic excitability, AP backpropagation, and synaptic stability.

A: *Scn2a*$^{+/fl}$ mice were injected with a dilute Cre virus, infecting a subset of neurons in PFC. Images are single 2PLSM optical section of transmitted laser light ("scanning-DIC") and mCherry fluorescence (red). Left, dashed circles highlight two neighboring Cre+ and Cre- neurons. Right, Cre+ neuron targeted for whole-cell recording with pipette from left-hand side. Image taken while in cell-attached configuration.

B: Peak dV/dt vs age in conditional *Scn2a* mice. dVdt measurements were made from CaMKII::*Scn2a*$^{+/fl}$ or *Scn2a*$^{+/+}$ mice at several ages and compared to developmental curve derived from constitutive mice. Note overlap with wild-type developmental curve at P18 and eventual overlap with *Scn2a*$^{+/-}$ curve at >P50 for CaMKII::*Scn2a*$^{+/fl}$ neurons. Neurons in *Scn2a*$^{+/fl}$ mice injected with dilute Cre virus were assessed after P55. Circles and bars are means ± SEM. *: $p < 0.01$, Mann-Whitney.

C: Dendritic calcium imaging as in Fig. 2C, except in CaMKII::*Scn2a*$^{+/fl}$ or $^{+/+}$ cells.

D: Transient amplitude is plotted for the first of 5 bursts (left) and area under the curve from stimulus onset to stimulus onset + 500ms (right) in CaMKII::*Scn2a*$^{+/+}$ (n = 9 cells) or CaMKII::*Scn2a*$^{+/-}$ (n = 8 cells). Circles and bars are means ± SEM. *: $p < 0.05$, Mann-Whitney.

E: AMPA:NMDA ratio between CaMK-Cre:*Scn2a*$^{+/+}$ and *Scn2a*$^{+/fl}$ littermates, and between Cre+ and Cre- neurons in *Scn2a*$^{+/fl}$ mice injected with EF1α-Cre. *: $p < 0.05$, Mann-Whitney.

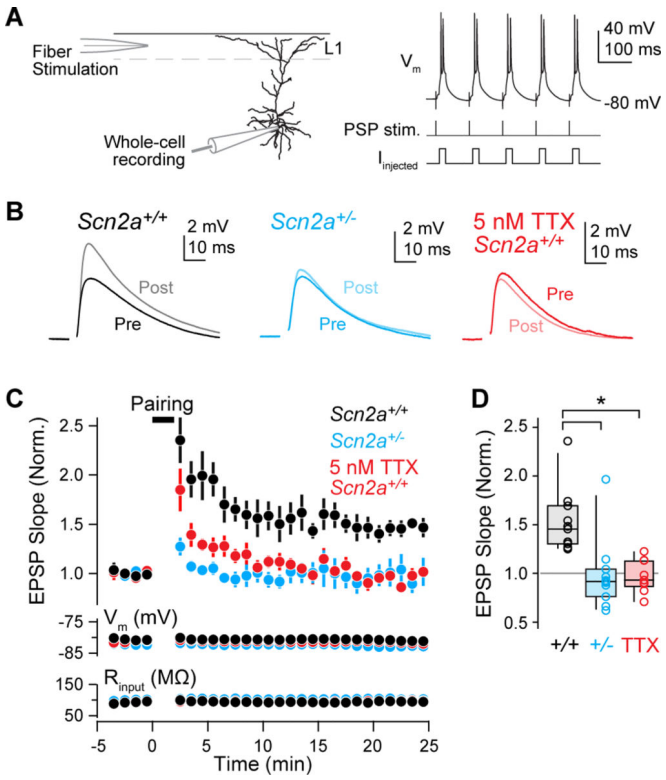

Figure 7: *Scn2a* haploinsufficiency impairs synaptic plasticity

A: Recording configuration for burst-based LTP experiments. Stimulating electrode was placed in layer 1 and synaptic stimulation was paired with somatic current-evoked AP bursts.

B: Example of EPSPs before and after LTP pairing protocol. Lighter shades are post-induction data (15–25 minutes after pairing). Stimulus artifact removed for clarity.

C: EPSP slope (first 2 ms), membrane potential (V_m) and input resistance (R_{in}) vs time before and after LTP induction. Circles and bars are mean ± SEM.

D: EPSC slope per cell in *Scn2a*$^{+/+}$ cells with and without TTX and *Scn2a*$^{+/-}$ cells. *: p = 0.0002, Kruskal-Wallis test; WT vs *Scn2a*$^{+/-}$: p = 0.0007, WT vs TTX: p = 0.002, Dunn's multiple comparisons test.

KEY RESOURCES TABLE

REAGENT or RESOURCE	SOURCE	IDENTIFIER
Bacterial and Virus Strains		
AAV5-Ef1α-Cre-mCherry	UNC Viral Core	N/A
Chemicals, Peptides, and Recombinant Proteins		
NBQX disodium salt	Tocris	0373
Tetrodotoxin-citrate	Alomone	T-550
(*R*)-CPP	Tocris	0247
Picrotoxin	Tocris	1128
Fluo-5F, Pentapotassium Salt, cell impermeant	Invitrogen	F14221
Alexa Fluor 594 hydrazide	Invitrogen	A10438
Prolong Gold Antifade with DAPI	Life Technologies	P36941
Experimental Models: Organisms/Strains		
Mouse: Ai14: 6;129S6-*Gt(ROSA)26Sor*$^{tm14(CAG-tdTomato)Hze}$/J	The Jackson Laboratory	JAX: 007908
Mouse: C57B6J	The Jackson Laboratory	JAX: 000664
Mouse: B6.Cg-Tg(Camk2a-cre)T29–1Stl/J	The Jackson Laboratory	JAX:005359
Mouse: *Scn2a*$^{+/-}$	M. Montal / E. Glasscock	PMID: 10827969, 28334922
Mouse: *Scn2a*$^{+/fl}$	This study	N/A
Software and Algorithms		
IGOR Pro	Wavemetrics	RRID:SCR_000325; v6.3
FIJI	https://fiji.sc/	RRID:SCR_002285
MATLAB	Mathworks	RRID:SCR_001622; v2016a
Python	pythn.org	RRID:SCR_008394; v3.5.2
IMARIS	Bitplane	RRID:SCR_007370; v6.3
Prism	Graphpad	RRID:SCR_002798; v8
Statview	SAS	v5.0.1
Ethovision	Noldus	RRID:SCR_000441